Characteristics of earthquake cycles: a cross-dimensional comparison from 0D to 3D

Meng Li[1], Casper Pranger[2,3], and Ylona van Dinther[1]

[1]Department of Earth Sciences, Utrecht University, Utrecht, Netherlands
[2]Department of Earth and Environmental Sciences, LMU Munich, Germany
[3]Department of Earth Sciences, ETH Zurich, Switzerland

Key Points:

- Models with dimension reduction simulate qualitatively similar quasi-periodic earthquake sequences with quantitative differences.
- Reduced influence of velocity-strengthening patches due to dimension reduction increases recurrence interval, slip and rupture speed.
- We provide guidelines on how to interpret lower-dimensional modeling results of interseismic loading and earthquake ruptures.

Corresponding author: Meng Li, `m.li1@uu.nl`

Abstract

High-resolution computer simulations of earthquake sequences in three or even two dimensions pose great demands on time and energy, making lower-cost simplifications a competitive alternative. We systematically study the advantages and limitations of simplifications that eliminate spatial dimensions, from 3D down to 1D in quasi-dynamic earthquake sequence models. We demonstrate that models in any number of spatial dimensions simulate qualitatively similar quasi-periodic sequences of quasi-characteristic earthquakes. Certain coseismic characteristics like stress drop and fracture energy are largely controlled by frictional parameters and thus their overall values are observed to be comparable across models of different dimensions. However, other observations are more strongly affected by dimension reduction. We find corresponding increases in recurrence interval, coseismic slip, peak slip velocity, and rupture speed. We find that these changes are largely explained by the elimination of velocity-strengthening patches that transmit loading conditions onto the velocity-weakening fault patch, thereby reducing the interseismic loading rate and enhancing the slip deficit. This is supported by a concise theoretical framework that explains some of these findings quantitatively. Given the computational efficiency of lower-dimensional models, this contribution aims to provide qualitative and quantitative guidance on economical model design and interpretation of modeling studies.

Plain Language Summary

Computer simulations are a powerful tool to understand earthquakes and they are often simplified to save time and energy. Dimension reduction - using 1/2D models instead of 3D models - is a commonly used simplification, but its consequences are not systematically studied. Here we find that both the overall earthquake recurrence pattern and the magnitude of stress changes on the fault caused by earthquakes remain relatively unchanged by model simplification by dimension reduction. However, some key observations such as the total slip and rupture speed achieved during an earthquake, as well as the precise recurrence interval are larger in lower-dimensional models. These changes are related to the elimination of lateral creeping regions that transmit stress onto the fault, which is an unavoidable consequence of the elimination of a physical dimension. We use simple theoretical calculations to reproduce these observations and justify this causal relationship. As simplified models are still popular due to their computational ef-

ficiency, this contribution helps their users to understand and anticipate the potential discrepancies of their results with respect to the three-dimensional situation that exists in nature. Therefore users can design their models and interpret their results with this work as a guideline.

1 Introduction

Earthquake sequences show statistical regularity in space and time (e.g., Utsu et al., 1995; Uchida & Bürgmann, 2019). Despite the complex patterns of earthquake occurrence observed over our limited observational window, evolution of fault slip has its internal time-dependence: stress accumulation due to persistent tectonic loading and stress release due to occasional seismic events make up an earthquake cycle. Understanding earthquake cycles is fundamental to recognize the recurrence of natural and induced earthquakes and ultimately helps to better assess long-term seismic hazard. Despite small to intermediate-size events regularly occurring on the same fault in nature (e.g., Chlieh et al., 2004; Prawirodirdjo et al., 2010) and generated quasi-periodically in scaled laboratory experiments (e.g., Rosenau et al., 2009; McLaskey & Lockner, 2014), the recurrence of large destructive earthquakes is hard to monitor due to their long recurrence interval. Moreover, natural observations are largely confined to the earth's surface, at some distance to the hypocenter. In addition, laboratory experiments are restricted by their scale and thus upscaling is often necessary to interpret their findings. Therefore, numerical models are well-suited to overcome these spatial-temporal limitations and improve our understanding of the Sequences of Earthquakes and Aseismic Slip (SEAS).

Numerical models featuring different degrees of complexity in different dimensions have been used to simulate earthquake cycles. They can be 0D (e.g., Madariaga, 1998; Erickson et al., 2008), 1D (e.g., Burridge & Knopoff, 1967; Gu & Wong, 1991; Ohtani et al., 2020), 2D (e.g., Lapusta et al., 2000; Van Dinther, Gerya, Dalguer, Mai, et al., 2013; Herrendörfer et al., 2018), 2.5D (e.g., Lapusta, 2001; Weng & Ampuero, 2019; Preuss et al., 2020) or 3D (e.g., Okubo, 1989; Lapusta & Liu, 2009; Barbot et al., 2012; Erickson & Dunham, 2014; Chemenda et al., 2016; Jiang & Lapusta, 2016). Generally, 3D models will produce results closest to nature among the listed methods. However, given that they are still very time and energy consuming (Uphoff et al., 2017), simplified model setups are still largely adopted by many researchers and may be the optimal choice to answer specific research questions (e.g., Allison & Dunham, 2018; Cattania, 2019). A key reason for the need of such simplifications is the extremely high resolution required in both space and time, while at least exploring sensitivities in forward modeling studies (Lambert & Lapusta, 2021). On top of that computational speed is particularly critical in situations where monotonous repetition of those forward models is required, for example, for inversion, data assimilation, physics-based deep learning, uncertainty quantification, and when dealing with probabilities, such as for probabilistic seismic hazard assessment (e.g., Weiss et al., 2019; Van Dinther et al., 2019). However, also when trying to understand coupled multi-physics or multi-scale feedback these approximations can be really useful (Van Dinther, Gerya, Dalguer, Corbi, et al., 2013; Allison & Dunham, 2018; Lotto et al., 2019; Ohtani et al., 2019; Petrini et al., 2020). To optimize computing resources, researchers have to define suitable model complexities before and during their numerical simulations. Therefore it becomes a common concern to what extent lower dimensional models can reproduce nature when compared to 3D models. How are the observed differences in results attributed to the corresponding dimension reduction? And under what circumstances is this simplification justified?

These questions have not yet been systematically addressed. Nonetheless, several contributions have considered various aspects of this problem, especially via the comparison between 2D and 3D models. Lapusta and Rice (2003); Kaneko et al. (2010); Chen and Lapusta (2019) all suggested ways to interpret their 2D results in more realistic 3D situations so that they can be directly compared to 3D results. By doing this, they could compare velocity-strengthening (VS) barrier efficiency in rupture propagation, seismic moment, and the scaling law for earthquake recurrence interval and seismic moment between 2D and 3D models in their studies. For the coseismic phase, simulations with dynamic rupture models of one single earthquake are generally conducted in 3D to obtain a full view of fault plane and thus give not enough attention to 2D models, except for the benchmark community. Harris et al. (2011) introduced two benchmark problems for dynamic rupture modelers where 3D simulations produced smaller ground motions (peak ground velocities) than the 2D simulations, in both elastic and plastic scenarios. Several contributions have also been made by earthquake cycle modelers. Chen and Lapusta (2009) suggested the 3D nucleation size would be larger than 2D by a factor of $\pi^2/4$. Chen and Lapusta (2019) also noted that their 2D models did not produce earthquakes that rupture only a part of the velocity-weakening (VW) patch, unlike what was happening in 3D. However, these findings are in pieces and some of them are lacking necessary reasoning. Here we fill in this gap by comparing earthquake cycle results across all dimensions from 0D to 3D, which includes all phases of the earthquake cycle, i.e., interseismic, nucleation, coseismic and postseismic.

We perform a systematic investigation of limitations and advantages of each dimension. By doing so, we compare physical characteristics and importance of different physical processes across dimensions both qualitatively and quantitatively. The aim of this paper is to serve as guidelines for modelers designing models and for all researchers interpreting results developed under necessary limitations. We first introduce the numerical method and the model setup of a strike-slip fault under rate-and-state friction. The code package is validated and benchmarked by Southern California Earthquake Center (SCEC) SEAS benchmark problems BP1-qd (Erickson, Jiang, Barall, Lapusta, et al., 2020) and BP4-qd (Jiang et al., 2021) (see Supporting Information S1). Next, we systematically compare interseismic and coseismic characteristics of our models from 1D to 3D, summarizing and quantifying their advantages and shortcomings. The numerical results are explained and supported by a series of theoretical calculations. Finally the computational cost is compared. In the discussions, we first discuss under what conditions 2D models can substitute 3D models. Related issues on the model choices of this research, limitations and future improvements as well as possible applications are also discussed.

2 Methods

To readily build models in different dimensions we exploit the flexibility of *Garnet*, a recently developed code library for the parallel solution of coupled non-linear multiphysics problems in earth sciences (C. C. Pranger, 2020). *Garnet* employs the classical second-order accurate staggered grid finite difference discretization of PDEs in space, formulated in a dimension-independent way and thus readily generalizable to higher or lower spatial dimensions. It also includes adaptive time stepping schemes of various orders of accuracy and other characteristics, all based on the linear multistep family of time discretizations. The library interfaces to PETSc (Balay et al., 1997, 2019b, 2019a) for linear and nonlinear solvers and preconditioners, to MPI (Forum, 2015) for coarse scale distributed memory parallelism and intermediate scale shared memory parallelism, and to Kokkos (Edwards et al., 2014) (and in turn OpenMP, POSIX threads, or CUDA) for fine scale concurrency. In this section we further introduce the equations and algorithms that define our study. To enable general comparison with established implementations, we take the 3D SCEC SEAS benchmark problem BP4-qd (Jiang et al., 2021) as a reference case for our models.

2.1 Physics

Under the assumption of static stress transfer, the momentum balance equation reads

$$\frac{\partial \sigma_{ij}}{\partial x_j} = 0 \ , \tag{1}$$

where ρ is density, σ_{ij} denotes the stress tensor, and v_i denotes the material velocity in the direction x_i ($i = 1, 2, 3$). Both gravity and inertia are ignored in our models. We will revisit the assumption of static stress transfer throughout the remainder of this section. Hooke's law in differential form relates stress rate $\dot{\boldsymbol{\sigma}}$ to strain rate $\dot{\boldsymbol{\varepsilon}}$ by

$$\dot{\sigma}_{ij} = K\dot{\varepsilon}_{kk}\delta_{ij} + 2G\left(\dot{\varepsilon}_{ij} - \frac{1}{3}\dot{\varepsilon}_{kk}\delta_{ij}\right) \tag{2}$$

with bulk modulus K, shear modulus G, and δ_{ij} Kronecker's delta symbol. We assume infinitesimal strain rate $\dot{\boldsymbol{\varepsilon}}$ as defined by

$$\dot{\varepsilon}_{ij} = \frac{1}{2}\left(\frac{\partial v_i}{\partial x_j} + \frac{\partial v_j}{\partial x_i}\right) \ . \tag{3}$$

For a fault with unit normal vector $\hat{n}$, the (scalar) normal stress σ_n (positive in compression) is given by the projection $\sigma_n = -\hat{n}\cdot\boldsymbol{\sigma}\cdot\hat{n}$, the shear traction vector $\vec{\tau}_s$ by the projection $\vec{\tau}_s = \boldsymbol{\sigma}\cdot\hat{n} + \sigma_n\hat{n}$, the scalar shear traction τ_s by the Euclidean norm $\tau_s = \|\vec{\tau}_s\|$, and finally the unit fault tangent $\hat{t}$ (which defines the orientation of the scalar fault slip V) by the normalization $\hat{t} = \vec{\tau}_s/\tau_s$, such that $\tau_s = \hat{t}\cdot\boldsymbol{\sigma}\cdot\hat{n}$. Further following Jiang et al. (2021), the fault is assumed to be governed by the rate-and-state friction law, which was initially proposed based on laboratory friction experiments by Dieterich (1979); Ruina (1983). We employ a regularization near zero slip velocity according to Rice and Ben-Zion (1996) and Ben-Zion and Rice (1997), so that the friction law that defines the relation between shear stress τ_s and normal stress σ_n on the fault is given by

$$\tau_s = a\sigma_n \text{arcsinh}\left(\frac{V}{2V_0}\exp\left(\frac{\mu_0}{a} + \frac{b}{a}\ln\left(\frac{\theta V_0}{L}\right)\right)\right) + \eta V. \tag{4}$$

The 'state' θ in turn is governed by the evolution equation

$$\dot{\theta} = 1 - \frac{V\theta}{L}, \tag{5}$$

corresponding to the so-called 'aging law' (Ruina, 1983). Symbols used in (4) and (5) include the reference friction coefficient μ_0, the reference slip rate V_0, the characteristic slip distance L, and the parameters $a > 0$ and b that control the relative influence of rate-strengthening and slip-weakening effects, respectively. The fault is velocity-weakening (VW) and potentially frictionally unstable when $a-b < 0$, and velocity-strengthening (VS) and generally frictionally stable when $a - b > 0$. Finally, the parameter η used in (4) refers to the 'radiation damping term' used in the quasi-dynamic (QD) approximation of inertia (e.g., Rice, 1993; Cochard & Madariaga, 1994; Ben-Zion & Rice, 1995; Liu & Rice, 2007; Crupi & Bizzarri, 2013) that is employed in earthquake cycle simulations to reduce the computational cost – even though it is known to introduce qualitative and quantitative differences compared to fully dynamic (FD) modeling results (Thomas et al., 2014). The damping viscosity $\eta = G/(2c_s)$ is equal to half the shear impedance of the elastic material surrounding the fault.

The nonlinear friction law (4) and evolution law (5) are solved in a point-wise fashion using a Newton-Raphson iteration for the slip rate V at a given stress $\boldsymbol{\sigma}$ (algorithm flowchart in Fig. S1). The problem is closed with an essential velocity boundary conditions $\vec{v} = \frac{1}{2}V\hat{t}$ on the fault, and remaining initial and boundary conditions are given in upcoming sections.

2.2 Model setup

Over the last decade, the SCEC has supported various code comparison projects to verify numerical simulations on dynamic earthquake ruptures (e.g. Harris et al., 2009, 2018). The SEAS benchmark project (Erickson, Jiang, Barall, Lapusta, et al., 2020; Jiang et al., 2021), launched in 2018, is an extension to evaluate the accuracy of numerical models simulating earthquake cycles. This benchmark initiative provides us with a platform to verify the earthquake cycle implementation in *Garnet*. Therefore, we build our models based on the setup of SEAS benchmark problem BP4-qd. This benchmark setup in turn facilitates the validation of our code package against other participating codes from the scientific community (see Supporting Information S1 and Jiang et al., 2021).

The BP4-qd describes a planar vertical fault embedded in a homogeneous, isotropic linear elastic medium, observing the physics described in section 2.1 (Fig. 1). The x, y, z axes are directions perpendicular to the fault plane, along the strike and along the dip, respectively. Following Jiang et al. (2021), the fault condition is prescribed at $x = 0$. The central part of the fault is assumed to follow the rate-and-state friction formulation

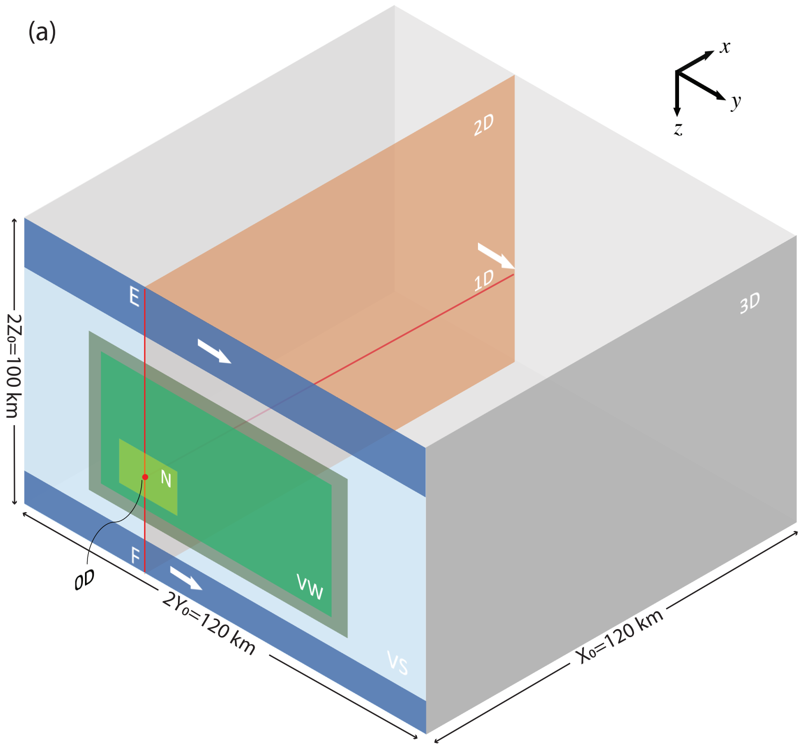

Figure 1. Numerical model setup of a vertical strike-slip fault embedded in an elastic medium: 3D setup of SEAS benchmark BP4-qd and its simplification to 2D, 1D and 0D. "VW" and "VS" denotes the VW (light green) and VS (light blue) patches, respectively. The transition between VW and VS patches is shown in dark green. Tectonic loading regions at the top and bottom of the fault (dark blue) are subjected to constant velocities (white arrows). "N" denotes the predefined nucleation zone (yellow) with higher initial slip rate and shear stress. Computational domain in 2D is reduced to xz-plane (orange) with 1D fault line "EF" along x-axis (red). Computational domain in 1D is reduced to x-axis (red) with 0D fault point "N" (red). In this case tectonic loading is applied at the far-away end with constant velocity (white arrow). Computational domain in 0D is fault point "N" without medium extent.

where a VW region is surrounded by a VS region. The top and bottom parts of the fault are not governed by rate and state friction and are instead subjected to a constant fault-parallel loading velocity V_p. Due to the symmetry respective to the fault plane and the resulting anti-symmetry of fault-parallel motion, the motion at the fault is taken to be relative to a fictitious oppositely moving domain that is not modeled. The computational domain is thus limited to the half space $x \geq 0$.

Since the benchmark proposes an infinitely large half space, the computational domain needs to be truncated to a finite domain when using a volumetric discretization. We use the computational domain $\mathbf{\Omega}(x, y, z) = [0, X_0] \times [-Y_0, Y_0] \times [-Z_0, Z_0]$ (Fig. 1), where X_0, Y_0, Z_0 are chosen sufficiently large to have negligible impact on the fault behavior (Jiang et al., 2021, see also Fig. S2). The top and bottom boundaries $z = \pm Z_0$ are prescribed to move at the same constant loading velocity V_p. The remaining three boundaries $x = X_0, y = -Y_0, y = Y_0$ mimic the conditions at infinity and are set to be traction-free.

The initial conditions are chosen to allow the fault to creep at the imposed slip velocity V_p in a steady state at $t = 0$ (Jiang et al., 2021), namely

$$\theta(t = 0) = \frac{L}{V_p} \ , \tag{6}$$

and

$$\tau_s(t = 0) = a\sigma_n \mathrm{arcsinh}\left(\frac{V_p}{2V_0}\exp\left(\frac{\mu_0}{a} + \frac{b}{a}\ln\left(\frac{V_0}{V_p}\right)\right)\right) + \eta V_p \ . \tag{7}$$

We define a highly stressed zone "N" in the VW patch with higher initial slip velocity V_i (Fig. 1) to ensure the first earthquake nucleates at that location when the computation starts. For this zone, the state variable θ keeps unchanged to achieve the high prestress, namely

$$\tau_s((y, z) \in N, t = 0) = a\sigma_n \mathrm{arcsinh}\left(\frac{V_i}{2V_0}\exp\left(\frac{\mu_0}{a} + \frac{b}{a}\ln\left(\frac{V_0}{V_p}\right)\right)\right) + \eta V_i \ . \tag{8}$$

This helps us to better compare the coseismic behavior across dimensions. All physical and numerical parameters are summarized in Table 1.

2.3 Spatial and temporal discretization

We choose a spatial discretization that ensures that the smallest physical length scale in the rate and state friction model – the cohesive zone size Λ – is always well resolved. This cohesive zone size Λ (Rubin & Ampuero, 2005; Day et al., 2005) is given

Table 1. Physical and numerical parameters

Parameter	Symbol	Value
Density	ρ	2.670 g/cm^3
Shear wave speed	c_s	3.464 km/s
Poisson ratio	ν	0.25
Shear modulus	G	32.0 GPa
Bulk modulus	K	53.4 GPa
Normal stress	σ_n	50 MPa
Loading rate	V_p	10^{-9} m/s
Width of rate-and-state fault	W_f	80 km
Length of uniform VW region	l	60 km
Width of uniform VW region	H	30 km
Width of VW-VS transition zone	h	3 km
Reference friction coefficient	μ_0	0.6
Reference slip rate	V_0	10^{-6} m/s
Characteristic slip distance	L	0.04 m
Rate-and-state direct effect	a	
- VW		0.0065
- VS		0.025
Rate-and-state evolution effect	b	0.013
Width of predefined nucleation zone "N"	w_i	12 km
Distance of nucleation zone to boundary	h_i	1.5 km
Initial slip rate		
- inside nucleation zone	V_i	10^{-3} m/s
- outside nucleation zone	V_p	10^{-9} m/s
Medium extent perpendicular to fault	X_0	*40*/*80*/120^a km
Half fault extent along strike	Y_0	60/*90*^{a} km
Half fault extent along dip	Z_0	50/*60*^{a} km
Grid size	Δx	500/*1000*^{a} m

^{a} Numbers in italic are used in parameter studies.

by

$$\Lambda = \Lambda_0 \sqrt{1 - \frac{V_r^2}{c_s^2}},$$
$$\Lambda_0 = \frac{9\pi}{32} \frac{GL}{b(1-\nu)\sigma_n},$$

where V_r is the rupture speed and c_s is the shear wave speed. Λ_0 is the upper limit of the cohesive zone size when $V_r \rightarrow 0$. The dynamic cohesive zone size Λ shrinks with increasing rupture speed V_r. We find that a high resolution is required for the seismogenic domain and its neighboring off-fault area, while it is not required at medium to large distances to the fault. To save time and energy, we consider a grid that is statically refined near the VW zone. Refinement is realized by deforming the regular grid and writing the governing equations in general rectilinear coordinates, thus preserving the 2^{nd}-order accuracy of the numerical method (C. C. Pranger, 2020).

We use adaptive time stepping to deal with the strong variation of the slip velocity and state variables in between interseismic and coseismic phases. The critically resolvable time scale is due to the evolution of the friction law (Eq. 5). Following Lapusta et al. (2000), we let the time step Δt be given by

$$\Delta t = \min\left\{\zeta \frac{L}{V_{\max}}, (1+\alpha)\Delta t_{\text{old}}, \Delta t_{\max}\right\} . \tag{9}$$

where ζ is a factor controlled by the material and frictional parameters. We also require the next time step not to be larger than $(1{+}\alpha)$ times the former time step Δt_{old} to avoid instability in the postseismic phase. A maximum time step size $\Delta t_{\max}$ is further needed to keep resolving the interseismic period in sufficient detail.

2.4 Model simplification by progressive elimination of dimensions

In this work we take a structured approach to dimension reduction, eliminating first the lateral along-strike dimension, then the vertical dimension, and finally the fault-perpendicular dimension. Each of these steps are illustrated in Fig. 1. For clarity, the assumptions and variables concerned in each dimension are summarized in Table 2.

In 2D, the model is simplified by excluding the along-strike fault direction (denoted in orange in Fig. 1). This means that the material and frictional properties, boundary and initial conditions are assumed to be homogeneous in this direction. That assumption thus omits the along-strike heterogeneity introduced by the bounding VS patches as well. Furthermore, motion along the dip v_z is omitted. In this way, any half plane cutting the fault vertically may be taken as representative of the the entire model. The computational domain can thus be reduced to $\mathbf{\Omega}(x,z) = [0, X_0] \times [-Z_0, Z_0]$. As a consequence, only the σ_{xy} and σ_{yz} components of the stress tensor are required to be evaluated in this anti-plane strain model. To allow a coseismic comparison we keep there the highly stressed nucleation zone defined in 3D and choose to model the plane cutting across this zone. The fault is collapsed to the line "EF" (denoted in red in Fig. 1). Another common 2D perspective includes the in-plane strain assumption that models motion in a horizontal plane cutting the fault. While this configuration models a more complete set of momentum balance and elastic constitutive equations than the out-of-plane configuration we have chosen, the differences are only expected to manifest as a slightly modified elastic loading and corresponding changes in friction and nucleation size. We therefore choose to use the vertical 2D configuration that keeps the top/bottom loading regions for better comparison.

In 1D, we further simplify the model by letting all fields be invariant along dip in which case only the shear stress component σ_{xy} and the velocity component v_y remain. We thus lose the possibility to model spatial variations of frictional properties as the fault reduces to a 0D point at $x = 0$ in the computational domain $\mathbf{\Omega}(x) = [0, X_0]$. We choose the fault "point" to be velocity weakening, corresponding to a location inside the predefined nucleation zone at "N" to facilitate coseismic comparison (denoted in red in Fig. 1). In this model we lose the along-dip fault extent, so that the original on-fault tectonic loading from the top and bottom is no longer possible. Instead it is added at the far-away boundary with a constant creeping rate there. To achieve a comparable tectonic loading rate inside the VW patch across dimensions, we adjust the domain size X_0 so that the shortest distance between the VW patch and the creeping boundary is the same as in higher dimensional models. Namely, we let X_0 equal to $(W_f - H)/2$.

In 0D, both the medium and the fault become the same point. In this model without medium extent, physical loading at medium boundaries is also impossible. Therefore a driving force that can be chosen arbitrarily has to be added to the system instead. This model will be further discussed in section 4.2 where the equivalence of 1D and 0D models will be illustrated.

Table 2. Simplifications in different dimensional models

Dimension	Unknowns	Simplifications
3D	$V, \theta; v_x, v_y, v_z, \sigma_{xx}, \sigma_{xy}, \sigma_{xz}, \sigma_{yy}, \sigma_{yz}, \sigma_{zz}$	No fault opening
2D	$V, \theta; v_y, \sigma_{xy}, \sigma_{yz}$	+ strike-slip only, along-strike invariant
1D	$V, \theta; v_y, \sigma_{xy}$	+ along-dip invariant
0D	V, θ	+ integral perpendicular to fault

3 Results and Analysis

Following the simplifications summarized in Table 2 and Fig. 1, this section compares the 3D to 2D and 1D results, where the fault is modeled in 2D, 1D and 0D, respectively. Starting from the long-term observations of the earthquake cycles, we compare the interseismic phase across dimensions. Facilitated by the same initial conditions and predefined nucleation zone, we then compare the coseismic phase by the observations of the first earthquake.

3.1 Interseismic phase

Regardless of dimension, we observe quasi-periodic earthquake sequences (Fig. 2). In one earthquake cycle, shear stress is first accumulated from minimum 25 MPa to maximum 35-42 MPa during the interseismic phase and then released in an earthquake (Fig. 2b). Accordingly, slip velocity also increases from locked rates of 10^{-17} m/s in 2/3D and 10^{-20} m/s in 1D to seismic rate 10^{0} m/s at the same time (Fig. 2a).

By dimension reduction, our simulated earthquakes become more and more characteristic. In 3D, all simulated earthquakes nucleate from one corner of the rectangular VW zone and rupture throughout it until the rupture front reaches the transition to the VS zone. However, not all earthquakes initiate from the same nucleation zone, as is suggested by the slip profile (Fig. 3a). Rather, the nucleation location alternates between the top-left and bottom-right corners, resulting in a periodic cycle of two earthquakes with slightly different slip and recurrence interval. Similar results in 3D of two or more characteristic earthquakes repeating as a group have also been reported by Barbot (2019), where several possible mechanisms are suggested for this poorly understood phenomenon.

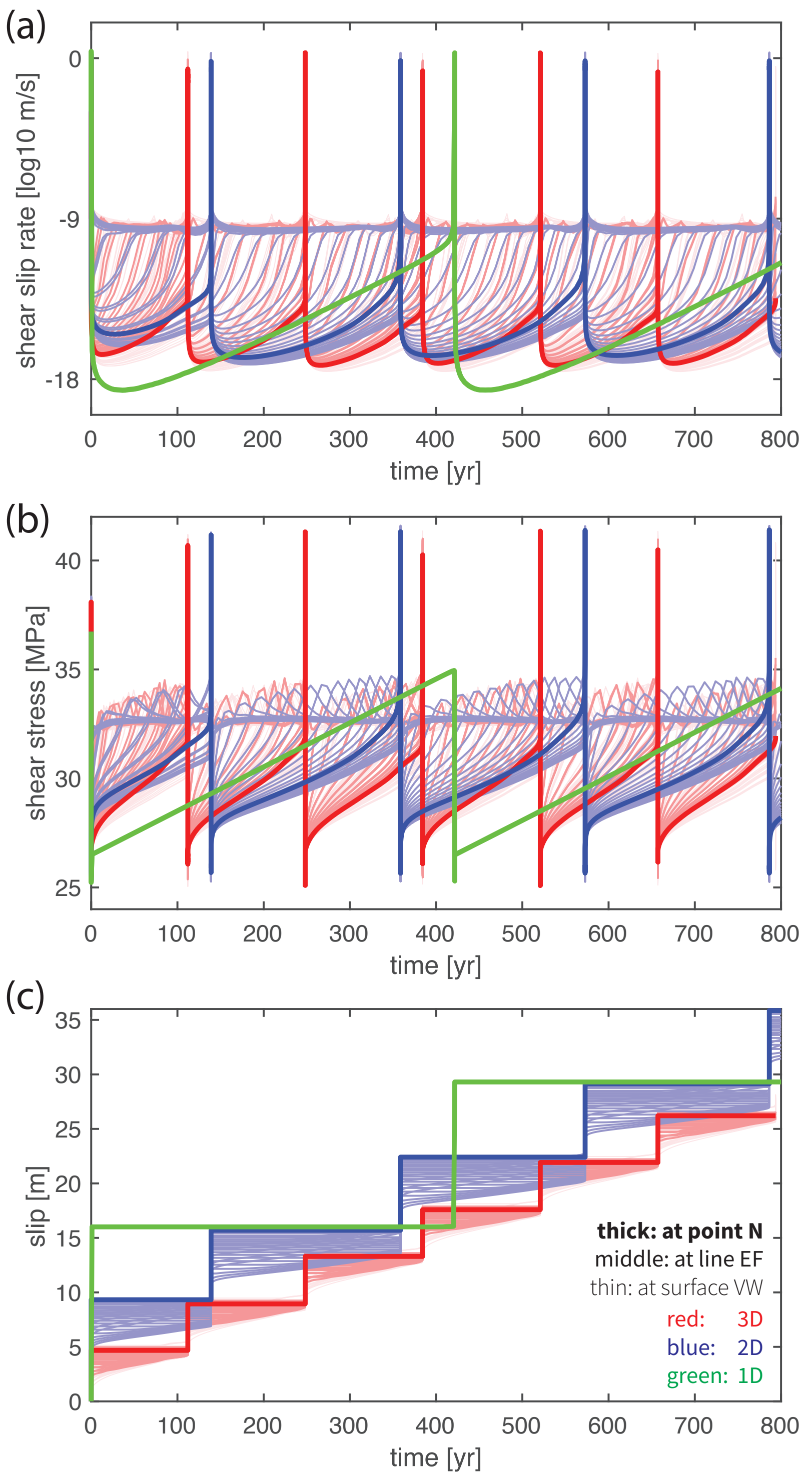

Figure 2. Comparison of the long-term time series of (a) slip rate, (b) stress and (c) accumulated slip in 1-3D models. The lines with different thicknesses and degrees of transparency are recorded at different locations on the fault, where the thick lines are recorded at the rim of the nucleation zone "N" of the sixth earthquake, the semi-thick lines along the line "EF" cutting across "N" vertically and the thin lines elsewhere in the VW patch (see Fig. 6).

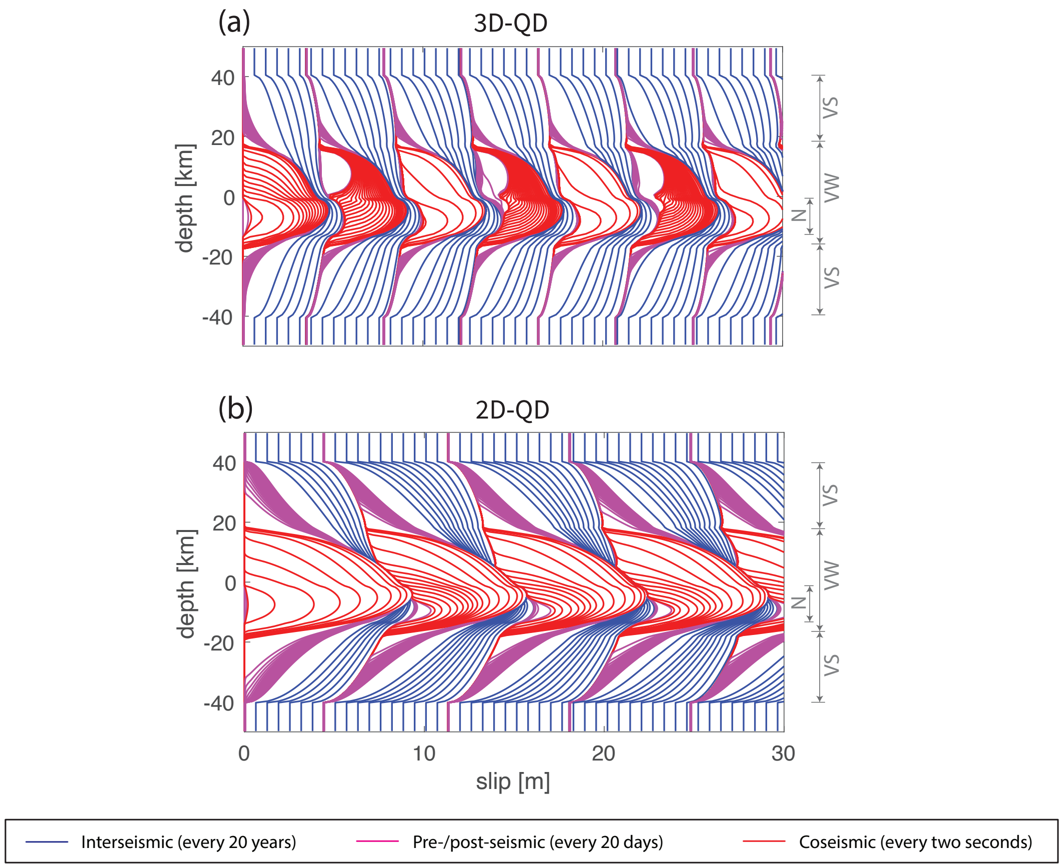

Figure 3. Cross-dimensional comparison of cumulative seismic and aseismic slip. The cumulative slip profile of (a) the 3D model and (b) the 2D model, along the dip direction "EF" cutting across the predefined nucleation zone "N" (see Fig. 1). "VW", "VS", "N" label the range of VW, VS and predefined nucleation zone. The interseismic phase is plotted every 20 years (blue), the pre- and post-seismic phase every 20 days (magenta) and the coseismic rupture every two seconds (red). Note that the slip contour distortions around a depth of -1.5 km and -13.5 km are introduced into these cumulative patterns by the predefined nucleation zone, whose properties increased the amount of slip in that zone for the first earthquake only.

In 2D, we find that the earthquakes are more periodic because they all nucleate from the same down-dip limit of the VW patch and rupture towards the up-dip limit, instead of alternately nucleating from the top and bottom sides (Fig. 3b). The earthquake size is also more identical with same recurrence interval. In 1D, we observe purely periodic, characteristic earthquakes of the same size (Fig. 2). This trend is because with fewer dimensions, interseismic loading pattern to the VW patch becomes simpler, so that the potential nucleation locations are also reduced. In 3D, earthquakes can potentially nucleate from four corners of the VW patch, which is reduced to two (top and bottom) in 2D and one in 1D. These observations demonstrate that as spatial dimensions are eliminated, the simulated results often exhibit a simpler spatio-temporal behavior.

Interseismic slip velocity and shear stress evolution depends on whether the observational point is inside the nucleation zone, at the nucleation rim (denoted by “N” in Fig. 6), or outside the nucleation zone (Fig. 2). Inside the nucleation zone tectonic loading is faster, therefore this portion of fault starts to creep at loading rate earlier. In the meantime, shear stress reaches its peak and gradually falls back to the steady-state level. Both slip velocity and shear stress are kept at this steady-state until the nucleation zone expands large enough (middle to thin lines that are to the left and above the thickest line in Fig. 2a, b). Outside the nucleation zone, at a point closer to the central VW patch that experiences slower loading, slip velocity and shear stress increase more slowly. This fault portion remains locked before the start of the next earthquake, i.e., slip velocity is always smaller than loading rate and shear stress lower than the aforementioned steady-state stress level (middle to thin lines that are to the right and below the thickest line in Fig. 2a, b). Only at the rim of the nucleation zone slip velocity and shear stress increase at a unique rate that allows for earthquake to occur as soon as respectively the loading rate and interface strength (as defined by Nakatani (2001)) are reached. As a result, no aseismic slip is accumulated at this location before earthquake starts (thickest lines in Fig. 2). These three patterns are shared in 2D and 3D models even though their nucleation zone shape and size are different. The 1D model with a 0D fault “point” mimics the nucleation rim of the higher dimensional models because slip initially becomes seismic without preceding aseismic accumulation. This is because in 1D an earthquake nucleates instantaneously as all points on the simulated fault plane reach the interface strength at the same time. We will see how the simple pattern of shear stress accumulation at this location helps in the later theoretical calculations.

By dimension reduction, simulated earthquakes reach larger slip and longer recurrence interval (Fig. 3). Different points of the fault experiences larger or smaller seismic slip during the earthquake, but the total slip (i.e., seismic slip + aseismic slip) in one earthquake cycle is generally constant throughout the fault plane (Fig. 3). It is also equal to the maximum coseismic slip because the maximum is achieved where the fault portion is locked outside the coseismic phase. This makes it, together with earthquake recurrence interval, a good indicator of the long-term earthquake cycle characteristics. In 3D, we observe earthquakes with average total slip of ~ 4.5 m and recurrence interval of ~ 135 yr (Fig. 3a). In 2D, the simulated values are ~ 6.8 m and ~ 215 yr, respectively, i.e., about 50% larger than in 3D (Fig. 3b). In 1D, they are 13.3 m and 420 yr, respectively, about three times as large as the 3D results and twice the 2D results (Fig. 2c). Note that in these numbers we excluded the slightly larger first earthquake that initiated at the predefined nucleation zone without tectonic loading.

These interseismic differences can largely be explained by the reduced presence of VS patches due to dimension reduction. During the interseismic phase, the VS patches are creeping at the loading rate so they do not accumulate stress. They only play a role in transferring the tectonic loading from the loading boundaries into the VW patch they surround. In other words, the VW patch is loaded directly by its surrounding VS patches rather than the loading boundaries, whether the bulk medium is simulated explicitly or not. This clarification is fundamental because in this way the VW patch in 3D is loaded from four sides, rather than only from the top/bottom where tectonic loading regions are located. While the VW patch in 2D is loaded from two sides, resulting in a lower interseismic loading rate inside the VW patch and hence a longer period before the next earthquake can nucleate. Given that the constant creeping rate in the VS patches is unchanged, the resulting larger slip deficit in the VW patch has to be made up by an earthquake with more slip. This is why larger earthquakes are observed in 2D. Quantitative calculations based on theoretical considerations, proving the analysis above, will follow in section 3.4.

That clarification also implies that the tectonic loading in the VW patch depends on the size of the VW patch itself instead of the size of the VS patches or the distance of the loading boundaries. The smaller the VW patch is, on average the stronger the loading will be. Therefore in 2/3D models the VW patch is actually not loaded at a distance from the predefined loading boundary but from much closer. This is simply not possible in 1D without VS patches. Even though in this case the distance between the VW fault and the far-away loading boundary is already chosen to be the same as in higher dimensions (in section 2.4) to make the stress rate directly caused by the loading boundaries comparable, the actual stress rate is proved to be inadequate. This is why larger slip and longer recurrence interval are still observed in 1D. Note that this explanation also suggests that different types of tectonic loading realization do not influence much the perceived stress rate inside the VW patch as long as it is surrounded by VS patches. This is supported by additional models with different types of loading at various distances from the fault, where similar earthquake recurrence intervals are obtained as long as the domain size is large enough (see Discussions and Table S1).

3.2 Observations of the first earthquake

We first analyze the coseismic behavior of the first earthquake where we have predefined the same nucleation zone as initial condition (Fig. 4a, c, e). Here we focus on the dynamic rupture behavior and use dimensional comparison to provide guidelines for dynamic earthquake rupture models. We then look at the sixth earthquake, a characteristic earthquake in the sequence, that experiences physical interseismic and nucleation processes (Fig. 4b, d, f). Via comparison to the first earthquake, we focus on the influence of the interseismic tectonic loading to the coseismic phase.

For the first event (Fig. 4a, c, e), the source time function at all locations within the VW patch takes the shape of Kostrov's solution (Kostrov & Das, 1988) with a short rise time and relatively long deceleration tail. As dimensions are reduced, the duration of the rise time decreases while the duration of the deceleration increases. The deceleration in 1D is the slowest, since the rupture does not interact with patches of different stress or strength properties that could decelerate it. For the same reason, it is impossible to observe rupture reflections in 1D. While the rupture reflection from the VW-VS boundary in 3D is clearly observable as a second slip velocity peak (Fig. 4a).

The peak slip velocity and the rupture speed are important earthquake characteristics that closely relate to rupture area size and seismic moment. We observe that peak slip velocities are all around the same order of magnitude around 10^0 m/s, but in 3D < 2D < 1D (Fig. 4a). The local peak slip velocity also increases while getting away from nucleation center. In 3D, the peak slip velocity is initially ~ 0.8 m/s in the predefined

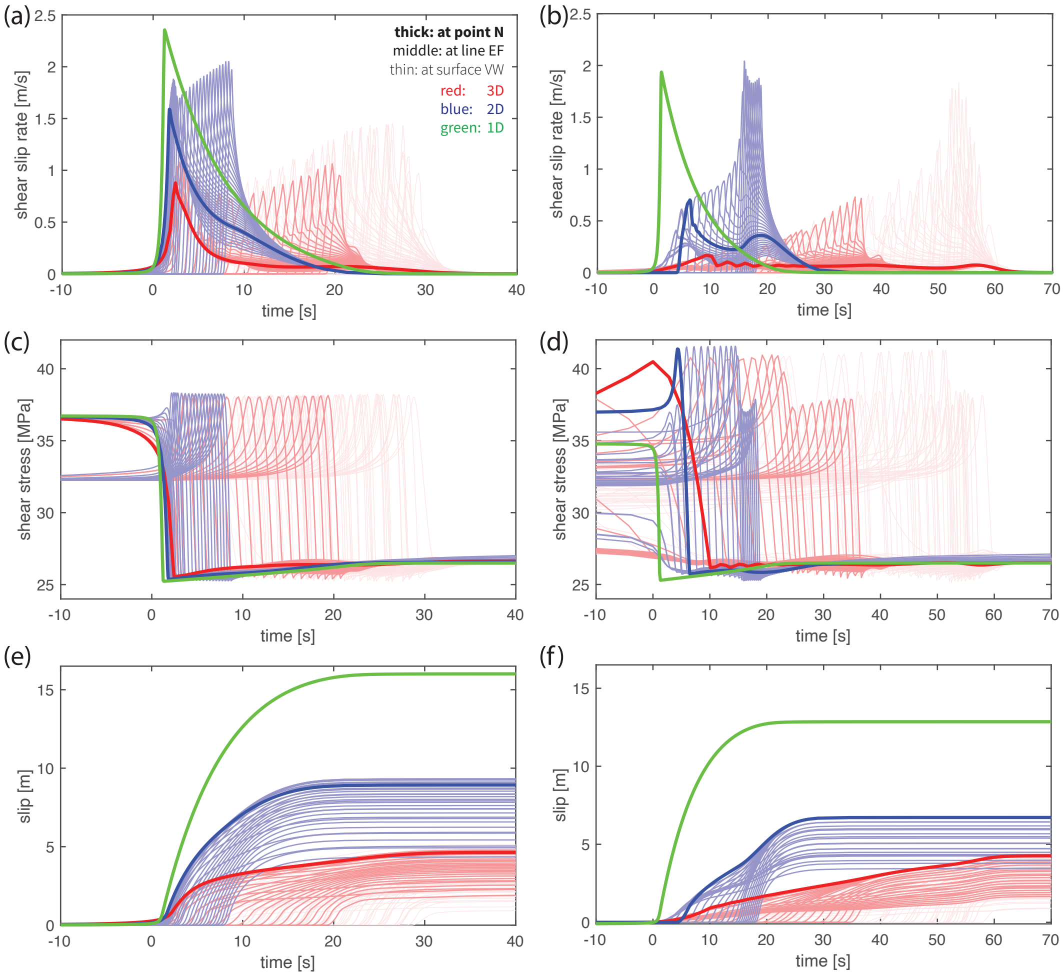

Figure 4. Comparison of the coseismic time series of (a, b) slip rate, (c, d) stress and (e, f) accumulated slip in 1-3D models. The first earthquake is shown in (a, c, e), and the sixth earthquake is shown in (b, d, f), where origin time is set at the onset of the respective earthquake. The lines with different thicknesses and degrees of transparency are recorded at different locations on the fault, where the thick lines are recorded at the nucleation location "N", the semi-thick lines along the line "EF" cutting across "N" vertically and the thin lines elsewhere in the VW patch (see Fig. 6a, c).

nucleation zone and gradually increases to its global maximum of $\sim$ 1.5 m/s. In 2D, the peak slip velocity is $\sim$ 1.6 m/s at the beginning and gradually increases to $\sim$ 2.0 m/s. In 1D, the maximum slip velocity is $\sim$ 2.4 m/s. We explain this increase with dimension reduction by considering the 2D models in a 3D perspective, where the 1D fault "line" is extended along strike to form a 2D fault surface in which the VW patch is infinitely long (e.g., Andrews et al., 2007). More importantly, every portion of the fault along this direction has to start to rupture at the same time and has the same rupture pattern. Therefore, contrary to 3D, no fracture energy is needed to rupture the unbroken part along strike, not to mention the inexistence of VS patches to absorb energy. Consequently energy is saved to achieve higher slip velocities. The same consideration also applies when considering the formulation of the 1D model in a 3D perspective, where the 0D fault "point" is extended to form an infinitely large, 2D fully-VW fault plane. Again, every portion of the fault has to rupture simultaneously with the same slip velocity and reach the same yield stress. No energy transfer is required at all to rupture the fault in both dip and strike directions and thus propagate the earthquake across it. Similarly, higher slip velocities are achieved (Kanamori & Rivera, 2006).

This explanation also suggests that the commonly observed periodic slow slip events cannot be reproduced in 1D models. When considered in the 3D perspective, the infinitely large VW patch namely leads to an infinite ratio of VW patch size (H) over nucleation size (h^*). While it is known that large enough H/h^* ratios always lead to seismic slip rates (Liu & Rice, 2007; Herrendörfer et al., 2018). This is because in this case the nucleation zone suddenly becomes infinitely large as soon as the 1D fault "point" starts to nucleate. This instability unavoidably leads to an earthquake (i.e., slip at seismic rate) instead of any slow slip events without additional damping. This extension is supported by a parameter study of hundreds of models in which no suitable frictional parameters are found allowing non-decaying slow-slip event simulation in 1D (Diab-Montero et al., in prep).

Rupture speed across dimensions shows lager variation than peak slip velocity. In 3D, the coseismic rupture lasts for $\sim$ 30 s. The rupture propagates faster in the horizontal direction than in the vertical direction and it experiences an acceleration in the last $\sim$ 10 s to reach near-shear speed (Fig. 5a). The rupture front takes $\sim$ 20 s to propagate along the vertical line "EF", at a near-constant speed of $\sim$ 0.83 km/s except for the first several seconds and the arrest. In 2D, the rupture takes only $\sim$ 10 s to reach

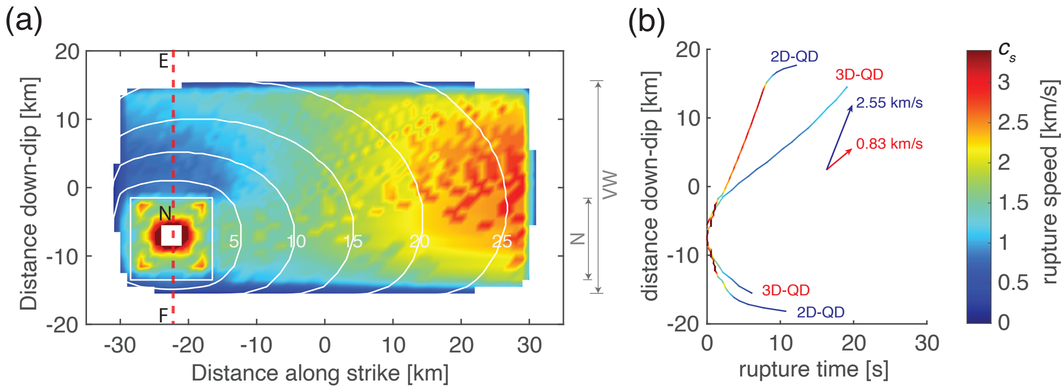

Figure 5. Comparison of coseismic rupture propagation. (a) The coseismic rupture speed of the first earthquake in 3D. The arrival time of the coseismic rupture front, which is measured when slip velocity reaching the seismic limit, is plotted every five seconds as contours. The central part of the fault plane is shown where white color means no seismic slip is observed. The red dashed line labels the observation line "EF" introduced in Fig. 1. Note that no reliable rupture speed is measured at rupture onset (left white near "N"). (b) The coseismic rupture front arrival time along the vertical line "EF" in 2D and 3D. The line color indicates the rupture speed under the same color scale as (a). Lines end at where slip rates drop below seismic threshold. The average rupture speed in the middle of propagation (i.e., except during nucleation and arrest) is measured as stated.

the up-dip limit starting from the same nucleation region (Fig. 5b). Thus coseismic duration is about 50% shorter than in 3D. Accordingly, the rupture speed of the stable part is $\sim$ 2.55 km/s, almost three times higher than in 3D. To explain these differences in rupture speed the same consideration used to explain peak slip velocities differences can be applied. In 2D models, no fracture energy needs to be overcome to rupture into the strike direction and hence more energy can be directed along dip, which allows the rupture to achieve higher speeds and thus shortens the rupture duration. For this reason 2D models are also seen rupturing deeper into the surrounding VS patches than 3D models. Given the difference between 2D and 3D models locate in the horizontal direction while the vertical direction keeps identical, our results suggest that the (in)existence of the horizontal VS patches has influence on the coseismic rupture behavior inside the VW patch, even in the vertical direction. We find this even evident in additional models where a second rupture deceleration can be observed if the length of the VW patch is shortened to one fourth (see Discussions, Fig. 9c, h, i).

The stress drop $\Delta\tau$, the stress difference between the start and the end of an earthquake, and the fracture energy G_c, the surface area below the stress w.r.t slip profile (Fig. 6b, d) are important earthquake parameters. Given the same initial condition, the stress drop and fracture energy of the first earthquake are comparable in all dimensional models, both inside and outside the prestressed zone (Fig. 6b). Regardless of dimension and at all VW locations we first observe the shear stress increasing up to the yield stress and then it drops to a constant level corresponding to dynamic friction (Fig. 4c). Both the yield stress and the dynamic stress are comparable across dimensions. Therefore the difference between the two (i.e., strength excess + stress drop, also called breakdown stress drop $\Delta\tau_b$) is also similar. Note that the initial stress increase is not as large when getting close to the nucleation zone and it is nearly zero inside it. This shows that the nucleation zone has to reach the yield stress before the coseismic phase, which is usually lower comparing to the maximum achievable yield stress elsewhere. After the stress drop we then immediately observe a small stress increase that is similar in size across dimensions (Fig. 4c), as a result of momentum conservation following the stress drop at neighbouring locations. This is the transition from dynamic stress drop to static stress drop (e.g., Madariaga, 1976). The dynamic stress drop at different locations is accompanied by a similar size of slip (Fig. 6b), regarded as the characteristic weakening distance by the slip-weakening theory. After this distance, coseismic slip continues to accumulate until earthquake ar-

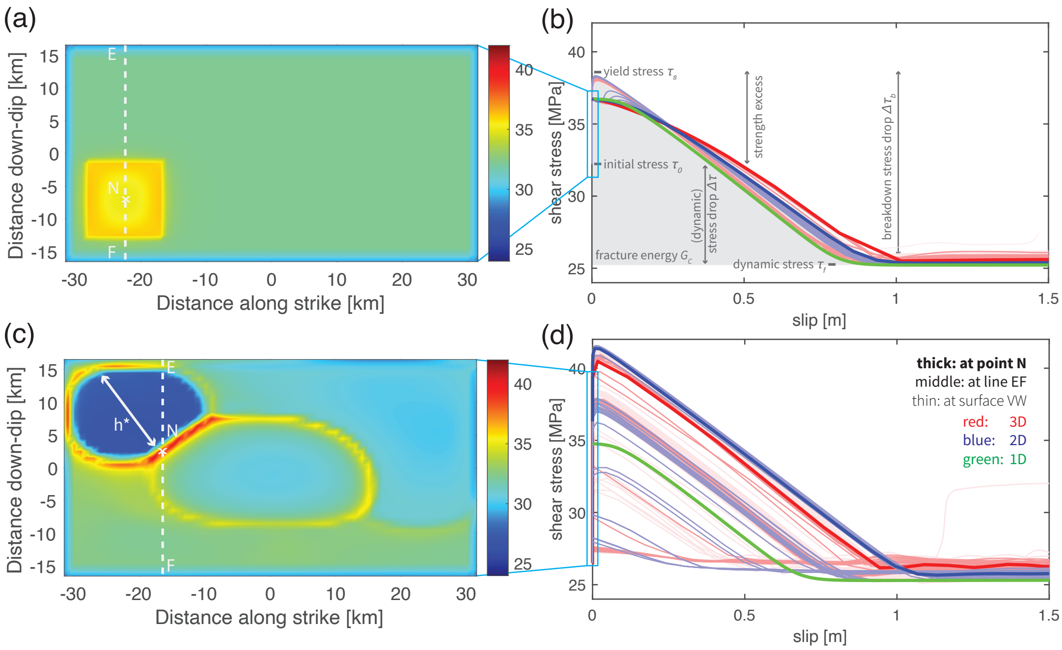

Figure 6. Cross-dimensional comparison of (a, c) the initial stress and (b, d) the coseismic stress evolution w.r.t. slip in 1-3D models for (a, b) the first earthquake and (c, d) the sixth earthquake. (a, c) The initial stress is measured when the maximum slip velocity reaches the seismic threshold. The nucleation size is denoted as h^*. Due to the high prestress, the coseismic slip of the first earthquake begins from the center of the nucleation zone. Whereas the coseismic slip of the sixth earthquake begins at the rim of the nucleation zone. Both are denoted by label "N". (b, d) The lines with different thicknesses and degrees of transparency are recorded at different locations on the fault, where the thick lines are recorded at point "N", the semi-thick lines along the line "EF" and the thin lines elsewhere in the VW patch (see panels a, c, respectively).

rests. The slip-weakening distance we measured here is between 0.8 m and 1.1 m, with 3D the longest and 1D the shortest. As a result, the fracture energy G_c (Fig. 6b) is also measured to be similar at all VW locations, and with 3D > 2D > 1D.

The differences of stress drop and fracture energy across dimensions are not strong, which is in line with expectations, since these earthquake parameters are largely controlled by the frictional properties and the normal stress (e.g., Rubin & Ampuero, 2005) that are homogeneous in this model. However, the modest systematic differences in, for example, the effective slip weakening distance shortening with dimension reduction, still indicates that the dynamics on the fault play a role in redistributing the earthquake energy budget, so that the stress drop and the slip weakening distance can change accordingly. This is more evident when the fault is shorted to one fourth its width where yield stress is observed decreasing while rupture propagates (see Discussions, Fig. 9j-m). In this case we also find that the observed yield stress decrease is accompanied with rupture deceleration. Lapusta and Liu (2009) observed the other two scenario's: they showed that the yield stress and slip-weakening distance increase with rupture acceleration while they are near constant when rupture propagates steadily.

3.3 Later earthquakes

For later earthquakes experiencing physical interseismic and nucleation processes, the comparison regarding the rupture speed and slip velocity remains qualitatively valid (Fig. 4b, d, f). However, we should point out that the rupture speed is overall about 50% slower than the first earthquake, resulting in twice as long rupture duration in both 2D and 3D models (Fig. 4b vs. a). This is because the central VW patch has been locked during the preceding interseismic phase during which it is healed to a much higher interface strength than its surrounding (Fig. 6c). The high interface strength limits rupture propagation into it. Not only the rupture speed is slowed down, but also the peak slip velocity is suppressed during this period of passing a high strength patch. Only until the rupture front has passed by it and is closer to the VW-VS transition can we observe the rupture speed and peak slip velocity increasing again. Combining lower slip velocity and longer coseismic duration, the accumulated seismic slip is observed to be smaller than the first earthquake (Fig. 3, 4e vs. f). Given that the initial pre-stressed zone increases the average initial stress of the first earthquake and thus increases stress drop, it is expected the first event can have higher seismic moment and thus larger slip than later ones.

Furthermore, the stress-slip profile and fracture energy are no longer near-identical throughout the VW patch due to heterogeneous initial stress and yield stress distribution (Fig. 4d, 6d). Instead of being predefined uniform, the initial stress in later earthquakes are the result of the uneven interseismic tectonic loading and the nucleation process. The nucleation zone thereby has the lowest initial stress, whereas its rim has the highest values close to yield stress (Fig. 6c). Given the same level of dynamic stress after the earthquake (Fig. 6d), this nonuniform initial stress field also results in a nonuniform stress drop $\Delta\tau$. In addition, we observe the yield stress changes during rupture propagation, making the breakdown stress drop $\Delta\tau_b$ nonuniform as well (Fig. 4d, 6d). Compared to the first earthquake, the yield stress becomes higher near the central VW patch and lower closer to the VW-VS transition and it becomes lower on average. The fracture energy varies accordingly. This observation is consistent with the explanation above where we mentioned the central VW patch is hard to rupture into due to its high interface strength. By comparing to the first earthquake we have illustrated the importance of earthquake/loading history to the coseismic process in modifying the stress and energy profile. We see that even the yield stress cannot be simply defined by the frictional properties. The 1D model, lacking the space for nucleation and dynamic rupture, never reaches the predefined high stress again in later earthquakes. Although we stated earlier that 1D model mimics the nucleation rim of 2/3D models in the long term, lacking high enough yield stress makes it dissimilar to 2/3D simulations in the coseismic phase.

3.4 Theoretical considerations

To better analyze the similarities and understand the differences from 1D to 3D, we utilize theoretical calculations that can estimate the aforementioned characteristic observables to the first order.

3.4.1 Earthquake cycle parameters

We calculate earthquake recurrence interval and total slip by extending the 3D theoretical formulation in Chen and Lapusta (2019) to all other dimensions using the analytical crack models of Knopoff (1958) and Keilis-borok (1959).

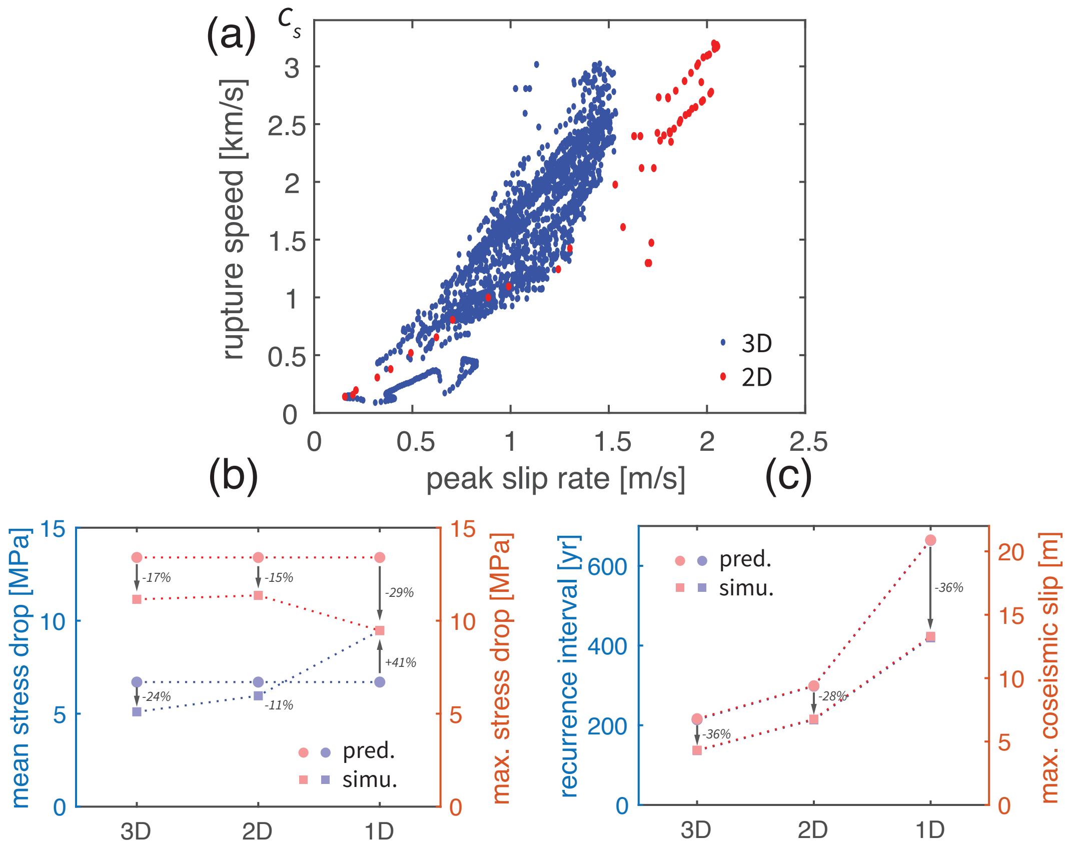

Figure 7. Comparison between theoretical predicted and numerically simulated results. (a) Interrelation between rupture speed and peak slip velocity in 3D (blue) and 2D (red) models. The local values are measured at different locations inside the VW patch. (b) Comparison between theoretically predicted (circle) and numerically simulated (square) average stress drop (blue) and maximum stress drop (red). The difference (in percentage) between calculated and simulated values is labeled aside. (c) Comparison between theoretically predicted (circle) and numerically simulated (square) recurrence interval (blue) and maximum coseismic slip (red). Same labels as in (b). Note that the markers in blue and red are largely overlapped in this panel.

The earthquake recurrence interval can be estimated when it is known how much stress will accumulate and what the stress rate is. However, as observed in the long-term time series (Fig. 2c), the stress accumulation pattern can be complicated and the stress level at the start of the next earthquake (i.e., the initial stress) is not uniform across the fault plane. In addition, the interseismic stress loading rate is not homogeneous within the VW zone. It is always loaded faster near the VW-VS transition and slower towards the central area, because the local stress rate is determined by the local strain rate that is largest at the strongest velocity contrasts. This means that both the accumulated stress and the interseismic stress rate vary from one point to another. Fortunately we notice that at some specific locations both can be calculated easily. At the end of the nucleation phase, the nucleation zone is expanded to its largest area at whose rim the highest initial stress is achieved that is close to the yield stress (e.g., location "N" in Fig. 6c). Since the accumulated stress is always released by the (dynamic) stress drop in the coseismic phase, it is also at these locations that the maximum stress drop is acquired. As the strength excess is small, the stress drop $\Delta\tau$ is close to the breakdown stress drop $\Delta\tau_b$ (Fig. 4c, d). Moreover, the interseismic stress loading there is close to linear as well (Fig. 2c). Therefore, by analyzing the stress accumulation pattern at location "N", we can estimate the maximum stress drop $\Delta\tau_{\max}$ and the recurrence interval T at the same time. This location is at the distance of h^* inside the VW patch since an earthquake can only nucleate when the creep penetrates this distance into the VW patch, where h^* is the nucleation size. In the end, the total slip D (i.e., aseismic + seismic slip) in one earthquake cycle, which equals to the maximum seismic slip, is estimated from the amount of the interseismic slip accumulated on the surrounding creeping VS patches.

First, the maximum stress drop $\Delta\tau_{\max}$ is approximated by the breakdown stress drop $\Delta\tau_b$, which is estimated from the stress difference between the two steady-state friction level during the interseismic and coseismic phase (Cocco & Bizzarri, 2002)

$$\Delta\tau_{\max} \approx \Delta\tau_b = b\sigma \ln\frac{V_{\mathrm{dyn}}}{V_p} \ , \tag{10}$$

where dynamic slip velocity V_{dyn} is approximated as 1 m/s for simplicity. Second, the stress rate is calculated at the desired location that is at the distance of h^* inside the VW patch (in 2D and 3D models, respectively, Rubin & Ampuero, 2005)

$$\begin{aligned} h^*_{\mathrm{2D}} &= \frac{2GLb}{\pi\sigma(b-a)^2} \\ h^*_{\mathrm{3D}} &= \frac{\pi^2}{4} h^*_{\mathrm{2D}} = \frac{\pi G L b}{2\sigma(b-a)^2} \end{aligned} \tag{11}$$

for mode III deformation in our models. The stress rate $\dot{\tau}_{h^*}$ there can be expressed as (Chen & Lapusta, 2019; Keilis-borok, 1959; Knopoff, 1958)

$$\dot{\tau}_{h^*} = C\frac{GV_p}{\sqrt{r^2-(r-h^*)^2}} \ . \tag{12}$$

For a fault segment of half-width r in 2D models or a circular fault of radius r in 3D models it has the same form with C a dimension-dependent constant being either $C_{3D} = 7\pi/24$ (Keilis-borok, 1959) or $C_{2D} = 1/2$ (Knopoff, 1958). This expression is directly applicable to our 2D models with $r = H/2$. While in 3D models, taken into consideration that the width of VW patch H is shorter than its length l, we can still apply this expression to our rectangular fault by assuming $r \approx H/2$. In 1D, the tectonic loading is applied from the far-away boundary. In this case we replace the whole denominator $\sqrt{r^2-(r-h^*)^2}$ by X_0, the distance between fault and the far-away loading boundary, with $C_{1D} = 1$. Third, by combining the interseismic stress rate and coseismic stress drop together we approximate the recurrence interval T by

$$T = \Delta\tau_{\max}/\dot{\tau}_{h^*} \ . \tag{13}$$

Finally, the total slip D, or the maximum coseismic slip, is estimated by

$$D = V_pT \ . \tag{14}$$

The theoretically predicted and numerically simulated maximum stress drop, recurrence interval and maximum coseismic slip are in agreement for all dimensions (Fig. 7b, c). This confirms the observed trend that longer recurrence interval and larger cosesimic slip are acquired due to dimension reduction. It also justifies our explanation that the larger coseismic slip is caused by the larger slip deficit during longer recurrence interval and the longer recurrence interval is caused by the lower interseismic stress rate.

The theoretically predicted values are a systematic overestimation by tens of percent. We notice that the relative difference is close for the recurrence interval and the total slip, indicating that the error in slip calculation (14) may be inherited from the recurrence interval calculation (13). The overestimation of the maximum stress drop $\Delta\tau_{\max}$ is a main contributor to this error, which is caused by using the breakdown stress drop as its approximation. Our simulations show that even for the locations at the nucleation rim (point "N" in Fig. 6c), a small stress increase still precedes the coseismic stress drop, resulting in $\Delta\tau_{\max} < \Delta\tau_b$ (Fig. 6d). Another source of the error is the underestimation of the interseismic loading rate $\dot{\tau}_{h^*}$. This is because when it is near the end of the interseismic phase, with the expanding nucleation zone that creeps, the stress rate at point "N" is much higher than in the original assumption (Fig. 2b). Despite the errors, these theoretical considerations well explained the simulated earthquake cycle parameters and their trend with dimension reduction as a first order approximation.

3.4.2 Dynamic rupture parameters

Unlike the earthquake cycle parameters, dynamic rupture parameters are variables on the fault. Therefore our theoretical calculations only serve as an approximation of their average values.

Our theoretical calculations cannot provide an estimate of the rupture speed. However, both laboratory experiments (Ohnaka et al., 1987) and theoretical considerations (Ida, 1973; Ampuero & Rubin, 2008) suggest that the peak slip velocity V_{peak} and the rupture speed V_r are interrelated by

$$V_r = \alpha_r V_{\mathrm{peak}} \frac{G}{\Delta\tau_b} \ , \tag{15}$$

where α_r is a factor on the order of 1. This positive correlation is confirmed by our simulations (Fig. 7a). We measured on average α_r of 0.82 in 3D and 0.65 in 2D for the first earthquake respectively, which is similar to what Hawthorne and Rubin (2013) measured (0.50-0.65) in their 2.5D simulations. The lower value of α_r in 2D shows that with dimension reduction higher slip velocity can be achieved under the same rupture speed.

The stress drop $\Delta\tau$ is not uniform across the simulated VW patch. Whereas the calculated stress difference from rate-and-state friction between the two steady states in the interseismic and coseismic phase is independent of dimension and location. Therefore it only provides an estimation of the average stress drop (Chen & Lapusta, 2019)

$$\begin{aligned} \overline{\Delta\tau} &\approx \tau(V_p) - \tau(V_{\mathrm{dyn}}) \\ &\approx \sigma[\mu_0 + (a-b)\ln(V_p/V_0)] - \sigma[\mu_0 + (a-b)\ln(V_{\mathrm{dyn}}/V_0)] \\ &= \sigma(b-a)\ln(V_{\mathrm{dyn}}/V_p) \ . \end{aligned} \tag{16}$$

The calculated average stress drop is slightly higher than the simulated results in 2D and 3D (Fig. 7b). However, it is still satisfying as a first order approximation for both models given that the contribution of the changing state has been ignored. The 1D model has a higher simulated average stress drop because the "average" loses its meaning in this case and the simulated value only represents where the earthquake nucleates. It is

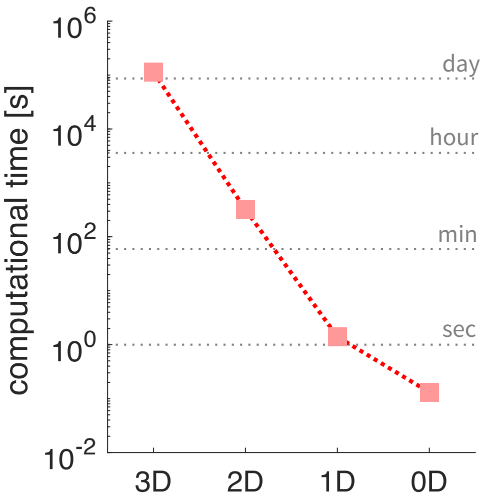

Figure 8. The average computational time of one earthquake cycle in 0D to 3D models, under the same resolution and domain size, with 12 CPUs Kokkos level parallelization.

well expected that higher stress drop is achieved here following the explanation in the previous section.

3.5 Computational efficiency

Lower dimensional models are computationally more efficient without losing the qualitative characteristics and the accuracy of certain earthquake parameters such as maximum slip velocity, maximum or average stress drop and fracture energy. To evaluate the computational efficiency of each model we measure the average computational time per earthquake cycle (Fig. 8). The 3D model takes 10^3 times longer time than 2D and 10^5 times longer than 1D. In the following discussions we will see that the 1D model can be further simplified to its 0D equivalent by removing the medium content. The 0D model will again save more than 90% running time compared to 1D. Note that these computations do not use distributed memory and therefore ignore related parallel scaling issues.

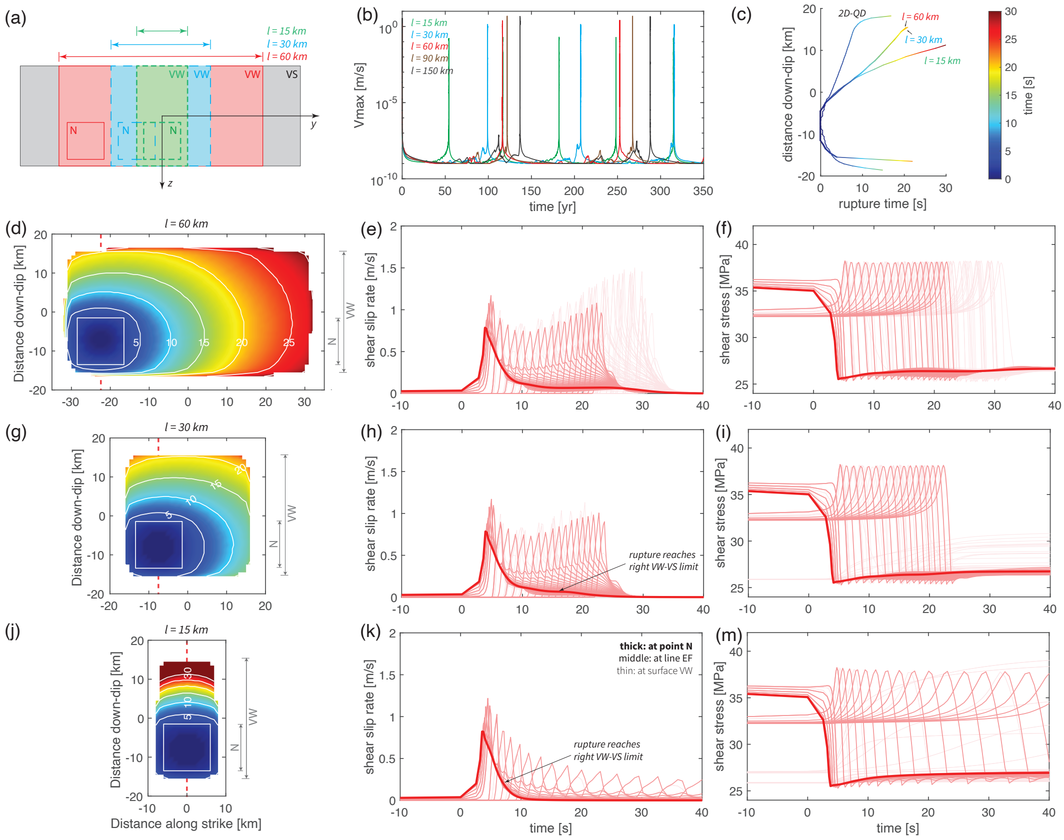

Figure 9. Comparison of the effects of fault length l (15 - 150 km) in 3D models: (d-f) 60 km, (g-i) 30 km, and (j-m) 15 km. (a) The varied VW patch sizes and varied locations of the predefined nucleation zone in three testing models with l from 15 km to 60 km. (b) The maximum slip velocity in multiple earthquake cycles for models with l from 15 km to 150 km. (d, g, j) The arrival time of the coseismic rupture front of the first earthquake, which is measured when slip velocity reaching the seismic limit. Only the central part of the fault plane is shown, where white color means no seismic slip is observed. Contours are plotted every five seconds. The red dashed line labels the observation line "EF" introduced in Fig. 1. (c) The coseismic rupture front arrival time along the vertical line "EF" under the same color scale. Lines end at where no seismic slip is observed. The rupture time of the corresponding 2D model is plotted as reference. (e, h, k) The time series of slip velocity in the coseismic phase of the first seismic event, in which origin time is set at the onset of this event. The lines with different thicknesses and degrees of transparency are recorded at different locations on the fault, where the thick lines are recorded at point "N", the semi-thick lines along the line "EF" and the thin lines elsewhere (see Fig. 1). (f, i, m) The time series of shear stress in the coseismic phase of the first seismic event, with the same line property.

4 Discussions

4.1 Under what conditions can 2D models substitute 3D models?

We have summarized model similarities over dimensions as well as analyzed how model discrepancies give rise to result differences. It is apparent that both quantitative and qualitative changes to these findings can take place more or less when a different model setup is used. Therefore it is meaningful to discuss in which situations dimension reduction can be used without considerable side effects or should be avoided even if computational efficiency is a factor. To simplify the question, we restrict our research to the most common discussion point: under what conditions can a 3D model be substituted by a 2D model? Obviously there is no such 2D model that can represent all 3D model setups, even if they can be simplified to the same model following our dimension reduction procedure (section 2.4). The reduced dimension always plays a role. To analyze the role of the along-strike dimension that is ignored in dimension reduction, we vary the VW patch length l and keep the VW patch width H fixed. By varying the VW patch length from 150 km to 15 km, we change the aspect ratio from 5:1 to 0.5:1 (Fig. 9). The fault (VW+VS patches) size and the computational domain (X_0, Y_0, Z_0) are kept unchanged as well as the predefined nucleation zone as an initial condition, which is always set at the left bottom corner with fixed distance h_i to the VW-VS boundary (Fig. 9a). This configuration benefits the coseismic comparison along the vertical line "EF" crossing this zone (Fig. 9c-m) to our 2D simulations (Fig. 4, 5).

In the long term, longer VW patches result in longer recurrence intervals (Fig. 9b). This is because the stress rate is lower comparing to a fault with a shorter VW patch. Given that the nucleation always starts from a corner of the rectangular VW patch, longer VW patches are mainly loaded from three directions as the tectonic loading from the other horizontal direction is farther away. From the perspective of theoretical considerations, the elongated fault geometry deviates from the circular fault assumption we used in 3D, while it is closer to the infinitely long fault assumption in 2D. Therefore theoretical calculations also suggest longer recurrence intervals to be expected. Consequently, by prolonging the VW patch length, we achieve longer recurrence intervals to fit better what is observed in 2D. In other words, higher aspect ratio faults in 3D are better represented by 2D models in the long term. However, even extending the 3D patch to 210 km still leads to shorter recurrence intervals in what is observed in 2D (Fig. 2), as interseismic loading remains more effective from three lateral sides than two.

On the other hand, a longer VW patch requires longer rupture propagation time along strike and thus longer coseismic duration, if the rupture speed remains unvaried (Fig. 9d, g). As explain before, 2D models can be seen as 3D models where theoretically no time is required to rupture along strike. In this sense, a longer VW patch length is not preferred to fit the short coseismic duration observed in 2D. However, even the shortest coseismic duration, observed with aspect ratio 1:1, is still much longer than 2D due to its low rupture speed. The rupture propagation time is not further shortened when the fault becomes even shorter. On the contrary, rupture speed is even largely decreased in the case with aspect ratio 0.5:1, resulting in a fairly long coseismic duration (Fig. 9c, j). This speed change happens after the rupture front reaches the horizontal VW-VS transition, confirming again that horizontal VW-VS interaction can change vertical rupture speed. Accompanying the rupture speed reduction, the slip velocity and the stress drop are reduced at the same time (Fig. 9k-m vs. e-f & h-i). This is dissimilar to how they are observed in 2D (Fig. 4a, c). In this sense, a shorter VW patch length is not favored either. In other words, medium aspect ratio (close to 1:1) fault is better represented by 2D models in the coseismic phase. Additionally, if only what happens along the vertical line “EF” in 3D is taken into consideration when compared to 2D, then all models with aspect ratio higher than 1:1 can be accepted. This is because we notice that the rupture propagation along the vertical line “EF” does not change much with respect to the fault length when the aspect ratio is larger than 1:1 (Fig. 9c). Nor do the slip velocity and coseismic slip change along this line (Fig. 9d-i).

To summarize, 2D models can better represent high aspect ratio faults in 3D for long-term observations and medium-to-high aspect ratio faults for coseismic observations. Whereas for coseismic observations there are definitely inevitable qualitative differences in between. Our conclusion suggests that when using empirical scaling relations to interpret 2D results from a 3D perspective, it is crucial to assume a suitable aspect ratio according to the corresponding research objective. Wesnousky (2008) summarized 36 historical natural earthquakes and found that they have similar rupture width but varied rupture length, resulting in varied aspect ratio from 0.7 to 12. The analysis in this study, covering the range 0.5 - 5, can therefore be useful to refer to when interpreting 2D simulations to 3D natural observations.

4.2 Model setup choices

We are going to discuss several model setup adjustments in this section to ensure that the conclusions drawn from our simulations are further supported and they can be generalized when located in a broader context. However, we should also acknowledge that there are research questions whose answers inherently require higher-dimensional spatial or geometrical complexity. We are not aiming at finding substitutes for such cases but rather to present the essential differences that are apparent in the simplest setup.

We started to build our models following the SEAS benchmark BP4-qd (Erickson, Jiang, Barall, Abdelmeguid, et al., 2020) and inherited their frictional parameter a, b, L choice that was aimed to facilitate the benchmarking under rather low resolution (500 - 1000 km). To make up for this somewhat unnatural choice we have implemented (part of) this study using the frictional parameters in benchmark BP1 (Erickson, Jiang, Barall, Lapusta, et al., 2020). Those simulations confirmed the results presented in this paper under high resolution (25 - 50 m), indicating the possibility to generalize our conclusions to a broader frictional parameter range. These benchmarks also helped us to validate the code library *Garnet* and our models for usage in earthquake cycle modeling by comparing to other participated modelers (see Supporting Information S1).

Our choice of computational domain size is aimed to set all boundaries far away from the fault so that the influence of those artificial boundary conditions is kept minimal. This is justified by implementing our models with different domain sizes (X_0, Y_0, Z_0 as in Table 1). We show that the simulated earthquake cycles in both long term and coseismic phase are converging upon enlarging the medium thickness X_0 and the difference is negligible when $X_0 > 40$ km (Fig. S2).

Tectonic loading is usually applied in two different ways: directly on the fault plane (e.g., Kaneko et al., 2011) or indirectly at the far-away boundaries (e.g., Herrendörfer et al., 2018). Both types have been adopted by studies for different research purposes. We adopted tectonic loading at the top/bottom of the fault plane for 2D and 3D models following BP4-qd, but at the far-away boundary for 1D models due to dimensional restriction. During the coseimic period, the influence of tectonic loading is not noticeable because of the short duration. To test the influence in the interseismic phase we applied tectonic loading conditions (a) only on fault surface at top/bottom region with fixed fault width, (b) only on far-away boundary surface, (c) both (a) and (b). We modeled in 2D with gradually enlarged computational domain (Table S1). We find that the recurrence interval converges to a set value as the computational domain is enlarged and is hardly affected by the type of loading when the computational domain is large enough. This invariance with respect to loading condition is supported by our theoretical calculations (section 3.4). Because there we explained that the main loading force to the locked VW patch is from its surrounding creeping VS patches. No matter how the loading is applied, the stress rate inside the VW patch is only related to its dimension and independent of the size of the VS patches or the fault as a whole (Eq. 12). The velocity gradient perpendicular to the fault contributes to the loading process as well, but it is minimized for large enough computational domain where on-fault loading becomes dominant. Therefore both the interseismic and coseismic characteristics are not sensitive to what kind of loading boundary condition is applied.

As for the initial condition, we have also adopted a predefined highly-stressed zone within the VW patch following BP4-qd. Since the later earthquakes do not necessarily occur from the same location, this predefined zone facilitated the quantitative coseismic comparison across dimensions by forcing the first earthquake to nucleate from this same region. It is suggested by former studies that initial conditions have little effect on subsequent earthquakes (e.g., Takeuchi & Fialko, 2012; Allison & Dunham, 2018), therefore this special initial condition should not harm our findings in terms of earthquake cycle characteristics. In this study we observe that the accumulative slip contour distortions around a depth of -1.5 km and -13.5 km are introduced by the predefined nucleation zone, whose properties increased the amount of slip in that zone for the first earthquake (Fig. 3). However, for non-accumulative variables no influence from the initial condition is observed in later earthquakes. Nevertheless, the first earthquake is not relatively characteristic in an earthquake cycle even though some qualitative characteristics are still shared by later earthquakes. We have added analysis of the sixth earthquake across dimensions to make up for this.

We mentioned that since physical tectonic loading becomes unavailable in 0D models, an arbitrary "driving force" has to be added to the system instead. To facilitate comparison, we can integrate the strain rate along the x direction in 1D models and use it to drive the 0D system. This is how the well-known "spring-slider" model is built (Burridge & Knopoff, 1967). Such a 0D model is mathematically equivalent to the 1D model. This is because the static momentum balance equation (Eq. 1) in 1D reduces to $\partial\sigma_{xy}/\partial x =$

0, i.e. $\sigma_{xy}(x,t) = \sigma_{xy}(t)$ – shear stress is time-varying but spatially constant. Combined with the 1D elastic constitutive equation, the time derivative of stress is given by

$$\dot{\sigma}_{xy} = G\frac{V_p - V}{X_0}. \tag{17}$$

Since this is an analytical simplification, the resulting model behavior is expected to remain the same. In this case 0D models are to replace 1D models due to their computational efficiency (Fig. 8). Nevertheless, when heteogeneity, inelastity and/or inertia are considered, the explanation above no longer holds, then 0D and 1D models have to be treated separately (e.g., C. Pranger et al., 2021).

4.3 Implications

We are the first to systematically study and quantify similarities and differences of how models in different dimensions simulate earthquake sequences. While large-scale parallel computing can be exploited to reduce the time to solution of 3D applications, this does not significantly lower the power consumption and consequently the monetary and environmental burden. Moreover, we find that the orders of magnitude difference of speed-up by dimensional reduction are so large, and can only be even larger when higher resolution is necessary, that they readily make the difference between being feasible for scientific and exploratory research or not. Hence lower dimensional models will likely remain essential for scientific exploration in the coming decades (Lapusta et al., 2019). Especially when the researcher's interest falls into the scope of what the lower dimensional models can handle, they are encouraged to use them as they could be hundreds to millions times faster than a 3D model with the same resolution. Even if 3D models are necessary for certain studies (e.g., Ulrich et al., 2019), simpler models can always be a useful starting point of an exploration. These results should serve as guidelines as to how to interpret the lower-dimensional modeling results with the effect of dimensional reduction always taken into account, rather than being regarded restricting model simplifications being adopted.

5 Conclusions

In this paper, we addressed a common concern of numerical modelers: how complex should my model be to answer my research question? Will dimension reduction qualitatively and quantitatively affect my results? And how? For this purpose we have systematically investigated different dimensional models from 0D to 3D in terms of their interseismic and coseismic characteristics and computational time for earthquake sequences and individual quasi-dynamic ruptures.

Our results demonstrate that all dimensional models simulate qualitatively similar quasi-periodic earthquake sequences. The stress accumulation pattern is much the same when observed at the rim of the nucleation zone. As for the earthquake cycle parameters, lower dimensional models produce longer recurrence intervals and hence larger coseismic slip. This trend is supported by our theoretical calculations where the effect of dimension reduction is well quantified. We observe that the VS patches play a crucial role in causing differences in the interseismic phase, because tectonic loading is effectively realized at the VW-VS transition by the velocity contrast between the creeping VS patches and the locked VW patch. As VS patches are removed when fault dimension is reduced, their absence reduces the interseismic stress rate inside the VW patch and thus increases the recurrence interval. The larger slip deficit built in this period will be transferred to a larger coseismic slip.

In the coseismic phase, we find that certain earthquake parameters such as the breakdown stress drop, (dynamic) stress drop and fracture energy can be accurately reproduced in each of these simpler models, because they are mainly governed by material frictional parameters. This finding is especially valid for the first earthquake without physical tectonic loading. For later earthquakes, the statement is only true on average of the VW patch. This is because the yield stress and effective slip weakening distance can change due to tectonic loading history. For the dynamic rupture parameters, lower dimensional models generally produce higher maximum slip velocities and higher rupture speeds. This is because less energy consumption will be required when fewer directions need to be ruptured into thus higher kinetic energy is reserved. Furthermore, we demonstrate that this interaction at the VW-VS transition can modify rupture speed, which is another crucial role the VS patches play in the coseismic phase. We find that the vertical rupture speed along the line "EF" in 3D is slowed down compared to 2D. It can be further slowed down when the fault length is shortened to one fourth its original length, proving the vertical rupture behavior is influenced by horizontal properties.

Finally, we highlight the power of lower dimensional models in terms of their computational efficiency. We find that under the same resolution 3D models require 10^3 times longer computational time than 2D, 10^5 times longer than 1D and 10^6 times longer than 0D models to simulate one earthquake cycle. Therefore dimension reduction can not only relieve the heavy energy-consuming simulations, but also improve the efficiency of projects that require monotonous repetitions of forward models. All the aforementioned findings are confirmed by our theoretical calculations, which suggest that differences during loading in the interseismic phase affect the subsequent coseismic phase. This paper may serve as guidelines to check in simplified models what results can be expected to be accurately modeled as well as what physical aspects are missing and how they are related to the discrepancies observed in the results. Not restrictive to this study, those theoretical considerations can be generally applied to other earthquake cycle models as well.

Acknowledgments

This study is part of the "InFocus: An Integrated Approach to Estimating Fault Slip Occurrence" project (grant number: DEEP.NL.2018.037) funded by NWO's (Dutch research council) DeepNL programme, which aims to improve the fundamental understanding of the dynamics of the deep subsurface under the influence of human interventions. ML designed and implemented the simulations, analyzed the data and wrote the paper. CP developed the code library *Garnet* and additional algorithms, and revised the paper. YvD conceived and supervised the study, analyzed the results and revised the paper. CP was supported by the European Union's Horizon 2020 Research and Innovation Programme under the ERC StG TEAR, grant no. 852992 and by Swiss National Science Foundation grant 200021-169880. We thank J. Jiang, B. Erickson and the SCEC SEAS benchmark project for the original numerical setup and the online platform. We thank H. Diab-Montero for the discussion on slow-slip events. We thank our colleagues, M. Goudarzi, F. Vossepoel, A. Niemeijer for their inspiring discussions and comments on this work. The code package *Garnet* is made accessible via repository `https://bitbucket.org/cpranger/garnet`. The models for this study can be found in the respective folders under `https://bitbucket.org/cpranger/garnet/src/meng-eejit/experiments/comparison/`. The data produced and analyzed in this study is available via `http://doi.org/10.5281/zenodo.4890931`.

References

Allison, K. L., & Dunham, E. M. (2018). Earthquake cycle simulations with rate-and-state friction and power-law viscoelasticity. *Tectonophysics*, *733*, 232–256.

Ampuero, J.-P., & Rubin, A. M. (2008). Earthquake nucleation on rate and state faults–aging and slip laws. *Journal of Geophysical Research: Solid Earth*, *113*(B1).

Andrews, D., Hanks, T. C., & Whitney, J. W. (2007). Physical limits on ground motion at yucca mountain. *Bulletin of the Seismological Society of America*, *97*(6), 1771–1792.

Balay, S., Abhyankar, S., Adams, M. F., Brown, J., Brune, P., Buschelman, K., ... Zhang, H. (2019a). *PETSc users manual* (Tech. Rep. No. ANL-95/11 - Revision 3.12). Argonne National Laboratory. Retrieved from `https://www.mcs.anl.gov/petsc`

Balay, S., Abhyankar, S., Adams, M. F., Brown, J., Brune, P., Buschelman, K., ... Zhang, H. (2019b). *PETSc Web page.* `https://www.mcs.anl.gov/petsc`. Retrieved from `https://www.mcs.anl.gov/petsc`

Balay, S., Gropp, W. D., McInnes, L. C., & Smith, B. F. (1997). Efficient management of parallelism in object oriented numerical software libraries. In E. Arge, A. M. Bruaset, & H. P. Langtangen (Eds.), *Modern software tools in scientific computing* (pp. 163–202). Birkhäuser Press.

Barbot, S. (2019). Slow-slip, slow earthquakes, period-two cycles, full and partial ruptures, and deterministic chaos in a single asperity fault. *Tectonophysics*, *768*, 228171.

Barbot, S., Lapusta, N., & Avouac, J.-P. (2012). Under the hood of the earthquake machine: Toward predictive modeling of the seismic cycle. *Science*, *336*(6082), 707–710.

Ben-Zion, Y., & Rice, J. R. (1995). Slip patterns and earthquake populations along different classes of faults in elastic solids. *Journal of Geophysical Research: Solid Earth*, *100*(B7), 12959–12983.

Ben-Zion, Y., & Rice, J. R. (1997). Dynamic simulations of slip on a smooth fault in an elastic solid. *Journal of Geophysical Research: Solid Earth*, *102*(B8), 17771–17784.

Burridge, R., & Knopoff, L. (1967). Model and theoretical seismicity. *Bulletin of the seismological society of america*, *57*(3), 341–371.

Cattania, C. (2019). Complex earthquake sequences on simple faults. *Geophysical*

Research Letters, *46* (17-18), 10384–10393.

Chemenda, A. I., Cavalié, O., Vergnolle, M., Bouissou, S., & Delouis, B. (2016). Numerical model of formation of a 3-d strike-slip fault system. *Comptes Rendus Geoscience*, *348* (1), 61–69.

Chen, T., & Lapusta, N. (2009). Scaling of small repeating earthquakes explained by interaction of seismic and aseismic slip in a rate and state fault model. *Journal of Geophysical Research: Solid Earth*, *114* (B1).

Chen, T., & Lapusta, N. (2019). On behaviour and scaling of small repeating earthquakes in rate and state fault models. *Geophysical Journal International*, *218* (3), 2001–2018.

Chlieh, M., De Chabalier, J., Ruegg, J., Armijo, R., Dmowska, R., Campos, J., & Feigl, K. (2004). Crustal deformation and fault slip during the seismic cycle in the north chile subduction zone, from gps and insar observations. *Geophysical Journal International*, *158* (2), 695–711.

Cocco, M., & Bizzarri, A. (2002). On the slip-weakening behavior of rate-and state dependent constitutive laws. *Geophysical Research Letters*, *29* (11), 11–1.

Cochard, A., & Madariaga, R. (1994). Dynamic faulting under rate-dependent friction. *pure and applied geophysics*, *142* (3), 419–445.

Crupi, P., & Bizzarri, A. (2013). The role of radiation damping in the modeling of repeated earthquake events. *Annals of Geophysics*, *56* (1), 0111.

Day, S. M., Dalguer, L. A., Lapusta, N., & Liu, Y. (2005). Comparison of finite difference and boundary integral solutions to three-dimensional spontaneous rupture. *Journal of Geophysical Research: Solid Earth*, *110* (B12).

Diab-Montero, H., et al. (in prep). An ensemble kalman filter for estimating slow-slip events and earthquake occurrences: A synthetic experiment.

Dieterich, J. H. (1979). Modeling of rock friction: 1. experimental results and constitutive equations. *Journal of Geophysical Research: Solid Earth*, *84* (B5), 2161–2168.

Edwards, H. C., Trott, C. R., & Sunderland, D. (2014). Kokkos: Enabling manycore performance portability through polymorphic memory access patterns. *Journal of Parallel and Distributed Computing*, *74* (12), 3202 - 3216. (Domain-Specific Languages and High-Level Frameworks for High-Performance Computing) doi: https://doi.org/10.1016/j.jpdc.2014.07.003

Erickson, B. A., Birnir, B., & Lavallée, D. (2008). A model for aperiodicity in earthquakes. *Nonlinear processes in geophysics*, *15*(1), 1–12.

Erickson, B. A., & Dunham, E. M. (2014). An efficient numerical method for earthquake cycles in heterogeneous media: Alternating subbasin and surface-rupturing events on faults crossing a sedimentary basin. *Journal of Geophysical Research: Solid Earth*, *119*(4), 3290–3316.

Erickson, B. A., Jiang, J., Barall, M., Abdelmeguid, M., Abrahams, L. S., Allison, K. L., ... Wei, M. (2020). Community code comparisons for simulating sequences of earthquakes and aseismic slip (seas): Exploring full dynamics and 3d effects. In *Scec annual meeting.*

Erickson, B. A., Jiang, J., Barall, M., Lapusta, N., Dunham, E. M., Harris, R., ... others (2020). The community code verification exercise for simulating sequences of earthquakes and aseismic slip (seas). *Seismological Research Letters*, *91*(2A), 874–890.

Forum, M. (2015). *Mpi: A message-passing interface standard. version 3.1.* Retrieved from https://www.mpi-forum.org/docs/mpi-3.1/mpi31-report.pdf

Gu, Y., & Wong, T.-f. (1991). Effects of loading velocity, stiffness, and inertia on the dynamics of a single degree of freedom spring-slider system. *Journal of Geophysical Research: Solid Earth*, *96*(B13), 21677–21691.

Harris, R. A., Barall, M., Aagaard, B., Ma, S., Roten, D., Olsen, K., ... others (2018). A suite of exercises for verifying dynamic earthquake rupture codes. *Seismological Research Letters*, *89*(3), 1146–1162.

Harris, R. A., Barall, M., Andrews, D. J., Duan, B., Ma, S., Dunham, E. M., ... others (2011). Verifying a computational method for predicting extreme ground motion. *Seismological Research Letters*, *82*(5), 638–644.

Harris, R. A., Barall, M., Archuleta, R., Dunham, E., Aagaard, B., Ampuero, J. P., ... others (2009). The scec/usgs dynamic earthquake rupture code verification exercise. *Seismological Research Letters*, *80*(1), 119–126.

Hawthorne, J., & Rubin, A. (2013). Laterally propagating slow slip events in a rate and state friction model with a velocity-weakening to velocity-strengthening transition. *Journal of Geophysical Research: Solid Earth*, *118*(7), 3785–3808.

Herrendörfer, R., Gerya, T., & Van Dinther, Y. (2018). An invariant rate-and state-dependent friction formulation for viscoeastoplastic earthquake cycle simulations. *Journal of Geophysical Research: Solid Earth*, *123*(6), 5018–5051.

Ida, Y. (1973). The maximum acceleration of seismic ground motion. *Bulletin of the Seismological Society of America*, *63*(3), 959–968.

Jiang, J., Erickson, B., Lambert, V., Ampuero, J.-P., Ando, R., Barbot, S., … others (2021). Community-driven code comparisons for three-dimensional dynamic modeling of sequences of earthquakes and aseismic slip (seas).

Jiang, J., & Lapusta, N. (2016). Deeper penetration of large earthquakes on seismically quiescent faults. *Science*, *352*(6291), 1293–1297.

Kanamori, H., & Rivera, L. (2006). Energy partitioning during an earthquake.

Kaneko, Y., Ampuero, J.-P., & Lapusta, N. (2011). Spectral-element simulations of long-term fault slip: Effect of low-rigidity layers on earthquake-cycle dynamics. *Journal of Geophysical Research: Solid Earth*, *116*(B10).

Kaneko, Y., Avouac, J.-P., & Lapusta, N. (2010). Towards inferring earthquake patterns from geodetic observations of interseismic coupling. *Nature Geoscience*, *3*(5), 363.

Keilis-borok, V. (1959, 11). On estimation of displacement in an earthquake source and of source dimension. *Ann. Geofis.*, *12*. doi: 10.4401/ag-5718

Knopoff, L. (1958). Energy release in earthquakes. *Geophysical Journal International*, *1*(1), 44–52.

Kostrov, B. V., & Das, S. (1988). *Principles of earthquake source mechanics.* Cambridge University Press.

Lambert, V., & Lapusta, N. (2021). Resolving simulated sequences of earthquakes and fault interactions: implications for physics-based seismic hazard assessment.

Lapusta, N. (2001). *Elastodynamic analyses of sliding with rate and state friction* (Unpublished doctoral dissertation). Harvard University.

Lapusta, N., & Liu, Y. (2009). Three-dimensional boundary integral modeling of spontaneous earthquake sequences and aseismic slip. *Journal of Geophysical Research: Solid Earth*, *114*(B9).

Lapusta, N., et al. (2019). Modeling earthquake source processes: from tectonics to dynamic rupture. In *Report to the national science foundation.*

Lapusta, N., & Rice, J. R. (2003). Nucleation and early seismic propagation of small and large events in a crustal earthquake model. *Journal of Geophysical Research: Solid Earth*, *108*(B4).

Lapusta, N., Rice, J. R., Ben-Zion, Y., & Zheng, G. (2000). Elastodynamic analysis for slow tectonic loading with spontaneous rupture episodes on faults with rate-and state-dependent friction. *Journal of Geophysical Research: Solid Earth*, *105*(B10), 23765–23789.

Liu, Y., & Rice, J. R. (2007). Spontaneous and triggered aseismic deformation transients in a subduction fault model. *Journal of Geophysical Research: Solid Earth*, *112*(B9).

Lotto, G. C., Jeppson, T. N., & Dunham, E. M. (2019). Fully coupled simulations of megathrust earthquakes and tsunamis in the japan trench, nankai trough, and cascadia subduction zone. *Pure and Applied Geophysics*, *176*(9), 4009–4041.

Madariaga, R. (1976). Dynamics of an expanding circular fault. *Bulletin of the Seismological Society of America*, *66*(3), 639–666.

Madariaga, R. (1998). Study of an oscillator of single degree of freedom with dieterich-ruina rate and state friction, laboratoire de géologie, ecole normale supérieure. *Unpublished Notes*.

McLaskey, G. C., & Lockner, D. A. (2014). Preslip and cascade processes initiating laboratory stick slip. *Journal of Geophysical Research: Solid Earth*, *119*(8), 6323–6336.

Nakatani, M. (2001). Conceptual and physical clarification of rate and state friction: Frictional sliding as a thermally activated rheology. *Journal of Geophysical Research: Solid Earth*, *106*(B7), 13347–13380.

Ohnaka, M., Kuwahara, Y., & Yamamoto, K. (1987). Constitutive relations between dynamic physical parameters near a tip of the propagating slip zone during stick-slip shear failure. *Tectonophysics*, *144*(1-3), 109–125.

Ohtani, M., Kame, N., & Nakatani, M. (2019). Synchronization of megathrust earthquakes to periodic slow slip events in a single-degree-of-freedom spring-slider model. *Scientific reports*, *9*(1), 1–9.

Ohtani, M., Nakatani, M., & Kame, N. (2020). Time to seismic failure induced by repeating sses in a single-degree-of-freedom spring-slider model. *Geophysical Journal International*, *224*(2), 1242–1255.

Okubo, P. G. (1989). Dynamic rupture modeling with laboratory-derived constitutive relations. *Journal of Geophysical Research: Solid Earth*, *94*(B9), 12321–12335.

Petrini, C., Gerya, T., Yarushina, V., van Dinther, Y., Connolly, J., & Madonna, C. (2020). Seismo-hydro-mechanical modelling of the seismic cycle: methodology and implications for subduction zone seismicity. *Tectonophysics*, *791*, 228504.

Pranger, C., Sanan, P., May, D., Le Pourhiet, L., & Gabriel, A.-A. (2021). Rate and state friction as a spatially regularized transient viscous flow law. *Earth and Space Science Open Archive*, 55. doi: 10.1002/essoar.10508569.1

Pranger, C. C. (2020). *Unstable physical processes operating on self-governing fault systems, improved modeling methodology* (Unpublished doctoral dissertation). ETH Zurich.

Prawirodirdjo, L., McCaffrey, R., Chadwell, C. D., Bock, Y., & Subarya, C. (2010). Geodetic observations of an earthquake cycle at the sumatra subduction zone: Role of interseismic strain segmentation. *Journal of Geophysical Research: Solid Earth*, *115*(B3).

Preuss, S., Ampuero, J. P., Gerya, T., & Dinther, Y. v. (2020). Characteristics of earthquake ruptures and dynamic off-fault deformation on propagating faults. *Solid Earth*, *11*(4), 1333–1360.

Rice, J. R. (1993). Spatio-temporal complexity of slip on a fault. *Journal of Geophysical Research: Solid Earth*, *98*(B6), 9885–9907.

Rice, J. R., & Ben-Zion, Y. (1996). Slip complexity in earthquake fault models. *Proceedings of the National Academy of Sciences*, *93*(9), 3811–3818.

Rosenau, M., Lohrmann, J., & Oncken, O. (2009). Shocks in a box: An analogue model of subduction earthquake cycles with application to seismotectonic forearc evolution. *Journal of Geophysical Research: Solid Earth*, *114*(B1).

Rubin, A. M., & Ampuero, J.-P. (2005). Earthquake nucleation on (aging) rate and state faults. *Journal of Geophysical Research: Solid Earth*, *110*(B11).

Ruina, A. (1983). Slip instability and state variable friction laws. *Journal of Geophysical Research: Solid Earth*, *88*(B12), 10359–10370.

Takeuchi, C. S., & Fialko, Y. (2012). Dynamic models of interseismic deformation and stress transfer from plate motion to continental transform faults. *Journal of Geophysical Research: Solid Earth*, *117*(B5).

Thomas, M. Y., Lapusta, N., Noda, H., & Avouac, J.-P. (2014). Quasi-dynamic versus fully dynamic simulations of earthquakes and aseismic slip with and without enhanced coseismic weakening. *Journal of Geophysical Research: Solid Earth*, *119*(3), 1986–2004.

Uchida, N., & Bürgmann, R. (2019). Repeating earthquakes. *Annual Review of Earth and Planetary Sciences*, *47*, 305–332.

Ulrich, T., Vater, S., Madden, E. H., Behrens, J., van Dinther, Y., Van Zelst, I., ... Gabriel, A.-A. (2019). Coupled, physics-based modeling reveals earthquake displacements are critical to the 2018 palu, sulawesi tsunami. *Pure and Applied Geophysics*, *176*(10), 4069–4109.

Uphoff, C., Rettenberger, S., Bader, M., Madden, E. H., Ulrich, T., Wollherr, S., & Gabriel, A.-A. (2017). Extreme scale multi-physics simulations of the tsunamigenic 2004 sumatra megathrust earthquake. In *Proceedings of the international conference for high performance computing, networking, storage and analysis* (pp. 1–16).

Utsu, T., Ogata, Y., et al. (1995). The centenary of the omori formula for a decay law of aftershock activity. *Journal of Physics of the Earth*, *43*(1), 1–33.

Van Dinther, Y., Gerya, T., Dalguer, L. A., Corbi, F., Funiciello, F., & Mai, P. M. (2013). The seismic cycle at subduction thrusts: 2. dynamic implications of geodynamic simulations validated with laboratory models. *Journal of Geophysical Research: Solid Earth*, *118*(4), 1502–1525.

Van Dinther, Y., Gerya, T. V., Dalguer, L., Mai, P. M., Morra, G., & Giardini, D. (2013). The seismic cycle at subduction thrusts: Insights from seismo-thermo-mechanical models. *Journal of Geophysical Research: Solid Earth*, *118*(12), 6183–6202.

Van Dinther, Y., Künsch, H. R., & Fichtner, A. (2019). Ensemble data assimilation for earthquake sequences: probabilistic estimation and forecasting of fault stresses. *Geophysical Journal International*, *217*(3), 1453–1478.

Weiss, J. R., Qiu, Q., Barbot, S., Wright, T. J., Foster, J. H., Saunders, A., ... others (2019). Illuminating subduction zone rheological properties in the wake of a giant earthquake. *Science advances*, *5*(12), eaax6720.

Weng, H., & Ampuero, J.-P. (2019). The dynamics of elongated earthquake ruptures. *Journal of Geophysical Research: Solid Earth*, *124*(8), 8584–8610.

Wesnousky, S. G. (2008). Displacement and geometrical characteristics of earthquake surface ruptures: Issues and implications for seismic-hazard analysis and the process of earthquake rupture. *Bulletin of the Seismological Society of America*, *98*(4), 1609–1632.